Polo-Like Kinase 1 phosphorylation tunes the functional viscoelastic properties of the centrosome scaffold

Matthew Amato[1], June Ho Hwang[2], Manolo U. Rios[1], Nicole E. Familiari[1], Michael K. Rosen[2], Jeffrey B. Woodruff[1,3]

1. Dept. of Cell Biology, UT Southwestern Medical Center, Dallas, TX 75390, USA
2. Dept. of Biophysics, Howard Hughes Medical Institute, UT Southwestern Medical Center, Dallas, TX 75390, USA
3. For correspondence: jeffrey.woodruff@utsouthwestern.edu

ABSTRACT

Centrosomes are membranelles organelles containing centrioles encapsulated by pericentriolar material (PCM). PCM nucleates microtubules that help position and segregate chromosomes during mitosis, yet how PCM resists microtubule-mediated forces is poorly understood at the material level. Here, we show that PLK-1 phosphorylation of SPD-5 tunes the dynamics and material properties of the PCM scaffold in *C. elegans* embryos. Microrheology of reconstituted PCM condensates reveals that PLK-1 phosphorylation decreases SPD-5 dynamics and increases condensate viscoelasticity. Similarly, in embryos, phospho-mimetic SPD-5 is less dynamic than wild-type SPD-5, which itself is less dynamic than phospho-null SPD-5. PCM built with phospho-null SPD-5 is smaller than normal, but its assembly can be partially rescued by reducing microtubule-dependent forces. The same is true for PCM built with phospho-mimetic SPD-5, yet the underlying causes are distinct: under force, phospho-null SPD-5 fails to assemble, while phospho-mimetic SPD-5 forms hyper-stable foci that fail to cohere into a uniform, spherical mass. Both mutants have defects with chromosome segregation and viability. Thus, tuning of SPD-5 phosphorylation optimizes PCM material properties to achieve correct PCM size, integrity, and function. Our results demonstrate how regulated chemical modification of a scaffolding protein modulates the material properties and function of a membraneless organelle.

1.0 INTRODUCTION

Mesoscale material properties like viscosity, elasticity, and strength emerge from the collective interactions between molecules. This is well understood for associative polymers solutions that undergo gelation or phase separation (Cohen, 1982; Flory, 1953). For example, chain length, valence, strength of interactions, and solubility are all well characterized to influence the material properties of engineered and biological polymer-based materials (Alshareedah et al., 2024; Ferry, 1980; Harmon et al., 2017). While this framework has been applied to understand subcellular structures, such as membraneless organelles (Banani et al., 2017; Lyon et al., 2021), the relationship between material properties and function of such structures is incompletely understood.

The centrosome represents an ideal model to investigate how material properties influence the function of membraneless organelles. The centrosome is a force-bearing structure composed of barrel-shaped centrioles that organize an amorphous proteinaceous matrix known as the pericentriolar material (PCM). PCM-nucleated microtubules help form the mitotic spindle, which segregates mitotic chromosomes during cell division (Gomes Pereira et al., 2021; Woodruff et al., 2014). PCM also nucleates astral microtubules that connect to cortically anchored motors, which generate force to position the mitotic spindle (Laan et al., 2012). If PCM integrity is disrupted, microtubule-based pulling forces can fragment it, leading to multipolar spindles and genomic instability (Maiato and Logarinho, 2014; Oshimori et al., 2006). These observations suggest that the material properties of the PCM are functionally important.

Understanding the molecular interactions within PCM could be informative for determining functionally important material properties. Upon entry into mitosis, PCM rapidly expands by accumulating scaffold proteins that then recruit client proteins needed for microtubule aster formation (Gomes Pereira et al., 2021). Major scaffold proteins have been identified in nematodes (SPD-5), insects (Cnn), and vertebrates (CDK5RAP2). These all contain numerous coiled-coil domains interspersed with disordered linkers (Hamill et al., 2002; Megraw et al., 1999) Polo-family kinase phosphorylation potentiates PCM maturation by promoting the self-association of these scaffold proteins (Conduit et al., 2014; Feng et al., 2017; Haren et al., 2009; Rios et al., 2024; Rios et al., 2025; Woodruff et al., 2015) In *C. elegans,* Polo-like Kinase (PLK-1) phosphorylation of SPD-5

at four sites (S530, S626, S653, S658) is important for SPD-5 multimerization and overall PCM maturation (Woodruff et al., 2015). Optical nano-rheology showed that *C. elegans* PCM can flow under shear stress, but only during its disassembly phase or when PLK-1 is inhibited (Mittasch et al., 2020). This result suggests that the material properties of the PCM are dynamic and are subject to cell cycle regulation by PLK-1. It is unclear if PLK-1 directly regulates the material properties of the PCM and whether properly tuned material properties are important for PCM function.

Here, we used cell-based and *ex vivo* biophysical assays, biochemical reconstitution, and microrheology to characterize how PLK-1 regulates the material properties of the PCM in *C. elegans*. We demonstrate that PLK-1 phosphorylation increases the viscoelastic moduli of reconstituted SPD-5 scaffolds in vitro. In embryos, we show that SPD-5 can transition between dynamically and stably associated states based on its phosphorylation status. A balance of these two states tunes the material properties of the PCM to optimize its mechanical integrity and ability to segregate chromosomes during mitosis.

2.0 Results

2.1 PLK-1 phosphorylation changes the dynamics and material properties of reconstituted PCM scaffolds

To investigate how PLK-1 phosphorylation changes the material properties of the PCM, we biochemically reconstituted PCM scaffold assembly *in vitro.* Previous reconstitution of micron-scale SPD-5 condensates required the use of macromolecular crowding agents, which dampened regulation by PLK-1 (Woodruff et al., 2017). More importantly, the presence of crowding agents has been shown to artificially affect the elasticity and viscosity of biomolecular condensates (Andre et al., 2023; Kaur et al., 2019). To circumvent these complications, we discovered conditions that permit SPD-5 condensation without using a macromolecular crowding agent. We found that SPD-5 in combination with its client protein TPXL-1 condenses into micron-scale droplets at near-physiological salt concentrations (75 mM KCl; Figure 1A, S1A,B). For the rest of this study, we refer to these reconstituted assemblies as “PCM condensates.”

93 Time-lapse imaging revealed that, after mixing of SPD-5, TPXL-1, and kinase dead
94 (KD) PLK-1, PCM condensates steadily grew. Incubation with constitutively active (CA)
95 PLK-1 initially enhanced PCM condensate assembly compared with the KD control (<10
96 min) (Figure 1B). Thus, PLK-1 activity, and not simply binding, promotes condensate
97 assembly, recapitulating PLK-1-mediated potentiation of PCM assembly seen in vivo
98 (Decker et al., 2011; Woodruff et al., 2015). At later time points, however, PLK-1 activity
99 inhibited PCM condensate growth, suggestive of kinetic arrest (Linsenmeier et al., 2022;
100 Ranganathan and Shakhnovich, 2020). Furthermore, PCM condensates incubated with
101 PLK-1(CA) appeared clustered, reminiscent of a colloidal suspension, whereas
102 condensates incubated with PLK-1(KD) were dispersed (Figure 1B,C).
103 Time-lapse imaging revealed that PCM condensates with PLK-1(KD) could fuse,
104 while condensates incubated with PLK-1(CA) could not fuse and remained clustered after
105 540 s (Figure 1C). Molecular rearrangement underlies droplet coalescence in soft matter
106 materials; therefore, we hypothesized that PLK-1 activity decreases the dynamics of PCM
107 condensates. Indeed, condensates with PLK-1(KD) recovered after photobleaching,
108 albeit at a low level, whereas condensates with PLK-1(CA) showed no recovery (Figure
109 1D, S1B). As an orthogonal approach, we measured persistence of SPD-5::RFP in
110 condensates after 4.3-fold dilution into a higher salt buffer (150mM KCl, 25mM Hepes pH
111 7.4). Unphosphorylated condensates lost considerable mass upon dilution, whereas
112 phosphorylated condensates largely maintained their mass (Figure 1E).
113 To confirm that dynamic changes conferred by PLK-1 activity were due to the
114 phosphorylation state of SPD-5 and not TPXL-1, we used phospho-mimetic SPD-5, which
115 contains serine to glutamic acid substitutions at 4 PLK-1 phosphorylation sites important
116 for PCM assembly (S530E, S627E, S653E, S658E; SPD-5(4E)) (Woodruff et al., 2015).
117 SPD-5(4E) condensates morphologically and dynamically recapitulated SPD-5(WT)
118 condensates treated with PLK-1(CA); both assembled smaller drops unable to fuse that
119 were resistant to dilution (Fig S1C, D). Furthermore, PLK-1 did not reduce TPXL-1
120 dynamics but rather increased them (Figure S1E). We conclude that phosphorylation of
121 SPD-5 directly decreases the dynamics of reconstituted PCM scaffolds and their ability to
122 fuse.
123

124 **2.2 Phosphorylation increases the viscoelasticity of reconstituted PCM scaffolds**

125 To quantify how phosphorylation changes the material properties of reconstituted
126 PCM, we used 100 nm beads to perform video particle tracking microrheology (VPT) of
127 SPD-5/TPXL-1 condensates incubated with PLK-1(CA) or PLK-1(KD)(Figure 2A). To
128 minimize effects from confinement, only beads located in the condensate center were
129 analyzed (see methods). Phosphorylation reduced the mean squared displacement
130 (MSD) of beads inside the condensates (n>17,000 trajectories; Figure 2B). Using the
131 Generalized Stokes-Einstein Relation, we expressed MSD in terms of the viscoelastic
132 modulus, which consists of viscous (G”) and elastic (G’) moduli as functions of frequency
133 (ω) (Figure 2C). Phosphorylation shifted the two moduli upward, indicating a transition to
134 higher viscoelasticity (Figure 2C), and shifted the first crossover point (where G’ = G”) to
135 the left, indicating emergence of elastic (solid-like) behavior at lower frequencies. In PLK-
136 1(CA) condensates, G’ and G’’ appeared to approach a second crossover point at a higher
137 frequency not accessible by our VPT analysis. We speculate that phosphorylation could
138 qualitatively change the rheological behaviors of SPD-5 condensates in addition to simply
139 quantitatively increasing their viscoelasticity (see Discussion). Next, we derived viscosity
140 (η) as a function of frequency using the relation η=G”/ω. Phosphorylation increased the
141 condensate viscosity at all frequencies (Figure 2D). The estimated zero-shear viscosity
142 (resting viscosity) of the condensates differed more than 8-fold: 31.8 Pa*s in the presence
143 of PLK-1(CA) vs. 3.8 Pa*s in the presence of PLK-1(KD).

144 The response of a viscoelastic material is dominated by elastic contributions on
145 short time scales and viscous contributions on longer time scales. The terminal relaxation
146 time characterizes the timescale when a material transitions from elastic to terminally
147 viscous behavior under applied stress and is defined as the inverse of the frequency at
148 the first G’-G” crossover point. Longer terminal relaxation times are associated with more
149 elastic, solid-like states. Phosphorylation increased the terminal relaxation time of SPD-
150 5/TPXL-1 condensates (4.6 s (CA) vs.1.03 s (KD); Figure 2C). Our microrheology data,
151 combined with FRAP and fusion assays, indicate that PLK-1 phosphorylation increases
152 the viscoelasticity of the PCM condensates, which leads to more solid-like PCM at
153 functionally relevant time scales. Furthermore, our data demonstrate that the dynamics
154 of SPD-5 correlate with viscoelasticity of PCM condensates (Figure 2E). We conclude

155 that phosphorylation-dependent tuning of SPD-5 dynamics determines the overall
156 viscoelastic behavior of PCM condensates.
157
158 **2.3 The phosphorylation state of SPD-5 affects its dynamics in metaphase-arrested**
159 **embryos**
160 We next investigated how phosphorylation impacts PCM material properties and
161 function in embryos. It is technically challenging to introduce beads into *C. elegans* PCM
162 and perform VPT. However, our in vitro system showed a strong correlation between
163 phosphorylation-induced changes in dynamics and material properties of SPD-5
164 condensates. Therefore, we sought to infer PCM material properties in embryos by
165 measuring SPD-5 dynamics. We generated embryos that express GFP-tagged, RNAi-
166 resistant transgenes of *spd-5* from an ectopic locus in the genome (Woodruff et al., 2015).
167 We mutated the four residues (S530, S627, S653, S658) known to be phosphorylated by
168 PLK-1 and important for PCM assembly to alanine (4A; phospho-null) or glutamic acid
169 (4E; phospho-mimetic) (Figure 3A). Importantly, this system allows us to test the effects
170 of mutant protein dosage: without RNAi, both mutant and wild-type SPD-5 co-exist, while
171 upon RNAi depletion of endogenous *spd-5*, only the mutant version is expressed
172 (Wueseke et al., 2016).
173 We assayed how the phosphorylation state of SPD-5 affects PCM scaffold
174 dynamics by performing fluorescence recovery after photobleaching (FRAP). To decouple
175 signal recovery contributed by replacement of existing material (dynamics) from
176 incorporation of new material from the cytosol (growth), we arrested cells in metaphase
177 when PCM stops growing (Laos et al., 2015). This is achieved by expressing a
178 temperature sensitive allele of *emb-30,* which encodes a subunit of the Anaphase
179 Promoting Complex (Furuta et al., 2000). After shifting embryos to 25°C for 15 min,
180 confocal imaging verified that embryos were arrested in metaphase and that PCM was
181 most stable 200-340 s post arrest. After 400 s following arrest, PCM disassembled,
182 indicating escape from arrest (Figure 3B). Therefore, we restricted our analysis to 200-
183 340 s post arrest.
184 In the presence of endogenous SPD-5 (no RNAi), GFP::SPD-5(4A) was the most
185 dynamic, recovering up to ~20%, whereas GFP::SPD-5(WT) and GFP::SPD-5(4E)

186 recovered at ~10% and ~5% respectively (Figure 3C,D). To test the effects of the mutant
187 proteins alone, we depleted endogenous SPD-5 using RNAi. Again, GFP::SPD-5(4A) was
188 the most dynamic, followed by WT then 4E (Figure 3C,D). RNAi treatment increased the
189 dynamics of SPD-5(4A), implying that it is partly stabilized by the presence of wild-type
190 protein (Figure 3D). On the other hand, RNAi treatment did not affect the dynamics of the
191 WT or 4E mutant. We noticed that PCM made with the SPD-5(4E) was highly irregular,
192 comprising an aggregate of several foci, rather than a cohesive, spherical assembly; the
193 nature of this behavior is not clear but could be a consequence of kinetic arrest (see
194 Discussion). These data indicate that a small, dynamic population of SPD-5 exists in
195 metaphase PCM. Furthermore, phosphorylation decreases the dynamics of SPD-5 within
196 PCM, consistent with our in vitro results.
197
198 **2.4 SPD-5 dynamics change with the cell cycle**
199 Our data indicate that PCM scaffold dynamics are affected by the phosphorylation
200 state of SPD-5. Given that PLK-1 activity changes during the cell cycle (Golsteyn et al.,
201 1995; Mittasch et al., 2020), we hypothesized that PCM scaffold dynamics are tuned
202 during the cell cycle. Due to the fast movement and growth of PCM, it is difficult to
203 measure dynamics using FRAP. Therefore, we used laser-induced extrusion to expel
204 PCM from the cell and measured its persistence, similar to our *in vitro* dilution assay
205 (Figure 1E). We performed extrusion by coating *C. elegans* embryos with calcofluor white,
206 a fluorescent dye that binds chitin and absorbs blue light, then using a short, focused
207 pulse of 405 nm laser light to create precise punctures in the embryo cortex. Application
208 of light pressure forced PCM out of the embryo into a dilute, controlled medium (Figure
209 4A). To ensure that the extrusion process itself does not damage the integrity of PCM, we
210 first extruded PCM (labeled with GFP::SPD-5) into low salt buffer (25 mM HEPES, 0 KCl).
211 PCM remained mostly stable for >1 hr (Figure 4B); thus, the wild-type PCM scaffold is not
212 damaged by extrusion. These results demonstrate that PCM is intrinsically stable and
213 does not require cytoplasmic factors for its maintenance in low salt conditions.
214 Extrusion into a high salt buffer (25 mM HEPES, 150 mM KCl) caused dissipation
215 of GFP::SPD-5 signal in a cell-cycle specific manner (Figure 4C,D). In extruded
216 interphase and metaphase cells, GFP integrated density rapidly declined initially and then

217 plateaued for up to 60 min, whereas, in anaphase, GFP integrated density monotonically
218 decreased and was no longer detected after ~10 min (Figure 4C-E). The total amount of
219 GFP signal remaining was higher in metaphase vs. interphase. However, normalization
220 of the signal revealed that departure rates were similar between metaphase and
221 interphase (Figure 4E). Our results indicate that PCM scaffold dynamics are subject to
222 cell cycle-dependent regulation: dynamics are relatively low in interphase and
223 metaphase, then increase dramatically in anaphase, which could facilitate PCM
224 disassembly. Furthermore, our data show the utility of extrusion to probe the dynamics
225 of growing or moving organelles.

226 We next wondered how disrupted phospho-regulation affects PCM persistence
227 following extrusion. We chose to focus on metaphase cells, when PCM is at its largest
228 and perturbations in stability, size, and integrity would be most prominent. In the presence
229 of endogenous SPD-5, GFP::SPD-5(4A) signal rapidly disappeared after extrusion
230 (Figure 4F), reminiscent of wild-type anaphase PCM. On the other hand, GFP::SPD-5(4E)
231 strongly persisted, much longer than GFP::SPD-5(WT) (Figure 4F). Considering that the
232 phosphorylation state of SPD-5 affected the dynamics of extruded PCM, we wondered if
233 PP2A, a PCM-resident phosphatase, could dephosphorylate PCM after extrusion and
234 affect its dynamics. Extrusion of metaphase PCM into a high salt buffer with 10 μM LB-
235 100, which inhibits PP2A (Magescas et al., 2019), showed higher persistence compared
236 to the control (Figure S2). This result suggests that PCM-associated PP2A can
237 dephosphorylate SPD-5 after extrusion and facilitate its departure. We conclude that
238 phosphorylation of SPD-5 increases the persistence of the PCM scaffold following
239 extreme dilution upon extrusion. These data support that phosphorylation decreases the
240 rate of SPD-5 dissociation from PCM, consistent with our in vitro results.

241 In the absence of endogenous SPD-5 (via *spd-5(RNAi)*), GFP::SPD-5(4A) signal
242 was lost even quicker (Figure 4F), again suggesting that wild-type SPD-5 can help
243 stabilize unphosphorylated SPD-5, as we saw in our FRAP assay. Unexpectedly, SPD-
244 5(4E) integrated density rapidly decreased initially and then stabilized over time; this
245 pattern was markedly different from the no RNAi condition. Higher resolution imaging
246 revealed that PCM made exclusively from SPD-5(4E) fragmented immediately following
247 extrusion, whereas wild-type PCM remained intact (Figure 4G). These 4E fragments

248 remained stable in fluorescence intensity but often drifted out of the imaging plane, thus
249 giving the appearance of lower overall GFP integrated density. We conclude that PCM
250 built with hyper-phosphorylated SPD-5 has compromised mechanical integrity at the
251 meso-scale: SPD-5(4E) can form small assemblies that are highly stable but poorly
252 connected to other assemblies. This lack of overall cohesiveness could explain the
253 irregular shape of PCM in *spd-5(4E)* embryos.
254
255 **2.5 The phosphorylation state of SPD-5 tunes the mechanical integrity of the PCM**
256 We then examined how the viscoelastic properties of PCM contribute to its
257 mechanical integrity, specifically its ability to withstand external forces without fracturing
258 or deforming. PCM must resist microtubule pulling forces, and defects in PCM scaffold
259 assembly can cause premature, force-driven disassembly of PCM (Rios et al., 2024). Our
260 in vitro experiments indicated the viscoelastic properties of the SPD-5 scaffold correlate
261 with SPD-5 dynamics, and that both are regulated by PLK-1 phosphorylation. Given that
262 SPD-5(4E) PCM without endogenous SPD-5 is structurally unsound when extruded from
263 embryos, we hypothesized that this PCM also suffers an assembly defect that could be
264 rescued by removing microtubule pulling forces by depolymerizing microtubules with
265 nocodazole.
266 Confocal imaging revealed that in the absence of endogenous SPD-5, PCM built
267 from GFP::SPD-5(4E) accumulated less mass relative to WT during mitosis (Figure S3A).
268 PCM was also smaller when SPD-5(4E) was expressed in the presence of endogenous
269 SPD-5 (Figure S3A). These changes in size were not due to differences in expression
270 levels or cell cycle lengths (Figure S3B,C). PCM built solely from SPD-5(4E) appeared
271 irregular and broken, in contrast to uniform, spherical wild-type PCM (Figure 5A). To test
272 if this is a material defect, we eliminated pulling forces by treating embryos with
273 nocodazole. Application of 40 μM nocodazole fully rescued the morphology of PCM in
274 *spd-5(4E)* embryos and partially rescued PCM mass (1.82-fold increase; $p < 0.005$), while
275 PCM mass in *spd-5(WT)* embryos was not affected ($p > 0.9$)(Figure 5A,B). Thus, *spd-*
276 *5(4E)* embryos have both a force-dependent and -independent deficiency in PCM
277 assembly. We conclude that hyper-phosphorylation of SPD-5 impairs its ability to build a
278 cohesive, full-sized scaffold.

279 Embryos expressing only SPD-5(4A) failed to build full-sized PCM, consistent with
280 previous studies (Woodruff et al., 2015). This phenotype was previously interpreted
281 exclusively as a defect in PCM assembly. However, treatment with 40 μM nocodazole
282 partially rescued PCM scaffold mass in these embryos (2-fold; $p < 0.005$)(Figure 5A,B).
283 Thus, similar to SPD-5(4E), SPD-5(4A) alone can also build a small amount of PCM that
284 is weak but is prematurely dissembled by pulling forces. Furthermore, this observation
285 supports the idea that PCM scaffold assembly and strength are interrelated. We suspect
286 that the underlying molecular basis for overall PCM weakness is different for the 4E and
287 4A mutants (see Discussion). We conclude that dysregulated phosphorylation of SPD-5
288 leads to force-dependent and –independent defects in PCM assembly.
289

290 **2.6 Proper SPD-5 phosphorylation is important for the fidelity of chromosome**
291 **segregation**

292 We hypothesized that PCM integrity defects caused by dysregulated
293 phosphorylation of SPD-5 could interfere with centrosome function. To test this, we
294 imaged chromosome segregation from metaphase until telophase in one-cell embryos
295 solely expressing *gfp::spd-5* transgenes. Chromosome segregation was normal in all *spd-*
296 *5(WT)* embryos. On the contrary, chromosome segregation was defective in 100% of *spd-*
297 *5(4A)* and 14% of *spd-5(4E)* embryos (Figure 6A,B,D). Defects included failure to position
298 mitotic chromosomes at the metaphase plate, lagging chromosomes during anaphase,
299 and appearance of extranuclear DNA in telophase (Figure 6B; Figure S4A,B). 34% of
300 *spd-5(4E)* embryos did not hatch (Figure S4C), and previous studies demonstrated that
301 *spd-5(4A)* embryos are largely inviable (Woodruff et al., 2015; Wueseke et al., 2016).
302 Thus, either hypo- and hyper-phosphorylation of SPD-5 interferes with chromosome
303 segregation and embryonic development.

304 Our extrusion data indicated that PCM built solely from SPD-5(4E) is mechanically
305 compromised, which could contribute to the mild chromosome segregation defect in these
306 embryos. If true, sensitizing the system by increasing mechanical load should exacerbate
307 PCM integrity and function defects in *spd-5(4E)* embryos. To test this, we increased
308 cortically directed microtubule pulling forces ~1.5-fold by depleting CSNK-1 (Panbianco
309 et al., 2008). In *spd-5(WT) + csnk-1(RNAi)* embryos, spindle rocking was exaggerated,

310 but PCM remained intact, as expected (Mittasch et al., 2020). In contrast, in *spd-5(4E) +*
311 *csnk-1(RNAi)* embryos, PCM was violently ripped apart and caused an increase in
312 chromosome segregation defects (Figure 6C,D; quantification of all defects is shown in
313 Figure S4A,B). Since CSNK-1 depletion is known to impair polar body extrusion (Flynn
314 and McNally, 2017), we excluded defects resulting from incorporation of the polar bodies
315 into aberrant additional nuclei. These data further demonstrate that PCM built from SPD-
316 5(4E) is mechanically unsound and cannot function in cases of increased load, unlike
317 wild-type PCM.

318 We next tested if chromosome segregation defects seen in *spd-5(4A)* embryos
319 were due to disrupted PCM mechanical integrity. Since chromosome segregation defects
320 are already severe in *spd-5(4A)* embryos, it is not productive to further sensitize the
321 system with *csnk-1(RNAi)*. Instead, we tested if decreasing microtubule pulling forces, via
322 *gpr-1/2(RNAi)*(Colombo et al., 2003) could rescue chromosome segregation. We saw a
323 30% reduction in segregation errors for *spd-5(4A)* embryos with reduced forces, whereas
324 chromosome segregation in wild-type embryos was not affected (Figure 6C,D). PCM size
325 was still reduced in *spd-5(4A)* embryos and spindle centration and rocking were defective,
326 indicating that the double RNAi knockdown was effective. We conclude that PCM built
327 with SPD-5(4A) is too weak to resist physiological microtubule pulling forces, which
328 ultimately affects the ability of PCM to assemble and function. Overall, our results
329 demonstrate that the mechanical integrity of the PCM scaffold is important for its function
330 in faithfully segregating mitotic chromosomes.

331

332 **3.0 Discussion**

333 The protein-rich PCM scaffold resists microtubule pulling forces needed to position
334 the mitotic spindle and segregate mitotic chromosomes. Here, we investigated how the
335 dynamics and material properties of the PCM scaffold influence its function in *C. elegans*.
336 Our results support a model whereby PLK-1 phosphorylation of SPD-5 reduces its
337 dynamics, which increases the viscoelasticity of PCM. Thus, PLK-1 phosphorylation
338 promotes the initial assembly of the SPD-5 scaffold and its emergent material properties.
339 Properly tuned viscoelasticity is required for the PCM to resist pulling forces and
340 segregate chromosomes during mitosis.

341 Viscoelastic materials exhibit a hybrid response to stress: an elastic spring-like
342 response that stores energy and a viscous response that dissipates energy over time.
343 Our results indicate that the PCM scaffold is viscoelastic, a property that is increased by
344 PLK-1 phosphorylation. Specifically, PLK-1 phosphorylation of the main scaffold protein
345 SPD-5 decreased its dynamics within PCM condensates and concomitantly increased the
346 viscous and elastic moduli of PCM condensates in vitro (Figure 1, 2). We saw similar
347 results in vivo, where SPD-5 dynamics and PCM material properties changed in relation
348 to phosphorylation status. Because both PLK-1 and its opposing phosphatase PP2A
349 coexist within the PCM, SPD-5 likely exists in both phosphorylated and dephosphorylated
350 states (Enos et al., 2018; Magescas et al., 2019). We propose that this balance tunes the
351 viscoelastic properties of the PCM scaffold to optimize function (Figure 7). Under-
352 phosphorylated SPD-5 is dynamic and can rearrange and depart, thus contributing to the
353 overall viscous, liquid-like behavior. On the other hand, phosphorylated SPD-5 is less
354 dynamic and cannot rearrange, thus contributing to the overall elastic, solid-like character
355 of PCM. This viscoelastic character allows PCM to assemble properly and resist
356 microtubule pulling forces during spindle assembly. Consistent with our model,
357 dysregulation of the phosphorylation state of SPD-5 is pathological, leading to premature
358 PCM disassembly, defective chromosome segregation, and embryonic lethality. PCM
359 built with solely phospho-null SPD-5 (SPD-5(4A)) assembles a thin layer of dynamic PCM
360 that is unable to resist microtubule pulling forces needed for full-scale assembly and
361 proper chromosome segregation. On the other hand, PCM built from solely phospho-
362 mimetic SPD-5 (SPD-5(4E)), exhibits a similar phenotype but is driven by a different
363 mechanism. This PCM is less dynamic, exhibiting multiple hyperstable foci, which cannot
364 cohere into a uniform PCM body and thus are broken apart by microtubule pulling forces.
365 Our results suggest that SPD-5 dynamics reflect the functionally relevant
366 viscoelastic properties of the PCM scaffold in embryos. Our *in vitro* data revealed that
367 PLK-1 activity decreased SPD-5 dynamics and concomitantly increased the
368 viscoelasticity of PCM condensates. *In vivo,* FRAP of PCM in metaphase-arrested cells
369 showed SPD-5 turnover in matured PCM over a biologically relevant time scale (140 s).
370 Thus, SPD-5 is dynamic, albeit at a low amount, consistent with molecular rearrangement
371 expected for a viscoelastic material. Our group previously demonstrated that PCM can

372 resist deformation induced by thermoviscous pumping at metaphase but not during
373 anaphase or when PLK-1 is inhibited (Mittasch et al., 2020). These material states align
374 with changes in SPD-5 dynamics we observed in the present study: SPD-5 became more
375 dynamic in anaphase (Figure 4C-E) or when underphosphorylated (e.g., 4A mutant)
376 (Figure 3C-D, 4F). Taken together these data support that SPD-5 dynamics are
377 responsible for the viscoelastic properties of PCM in embryos.

378 How important are these viscoelastic properties for function? PCM built from either
379 SPD-5(4A) or SPD-5(4E) mutants disrupted PCM dynamics and assembly and caused
380 chromosome segregation defects. A secondary question thus arises: is PCM scaffold size
381 or dynamics most critical for function? A previous study revealed that embryos expressing
382 a simpler SPD-5 phospho-mutant (S653A, S658A; called "2A"), failed to build full-sized
383 PCM like SPD-5(4A)(Ohta et al., 2021). Partial photobleaching revealed that GFP::SPD-
384 5(2A) and GFP::SPD-5(WT) both have similarly low dynamics, while GFP::SPD-5(4A)
385 has high dynamics (Figure S5A,B), as shown in other experiments. However, PCM built
386 from solely SPD-5(2A) properly segregates mitotic chromosomes (Ohta et al., 2021) while
387 PCM built from solely SPD-5(4A) cannot. This suggests that achieving correct scaffold
388 dynamics—and, by association, material properties—is more important than achieving
389 full size for PCM function.

390 Why would PCM built from solely phospho-mimetic SPD-5, which we hypothesize
391 is more viscoelastic than PCM built from phospho-null SPD-5, exhibit assembly defects?
392 Since PLK-1 phosphorylation is essential for mitotic PCM assembly (Conduit et al., 2014;
393 Decker et al., 2011; Haren et al., 2009; Lee and Rhee, 2011; Woodruff et al., 2015), it was
394 surprising that hyper-phosphorylation of SPD-5 led to PCM that was smaller and
395 irregularly shaped (Figures 3-6). Furthermore, this PCM existed as multiple foci unable to
396 cohere into a uniform body, that then fragmented into many stable packets upon extrusion
397 (Figure 4G) or under increased pulling forces (Figure 6). One hypothesis is that excessive
398 phosphorylation increases the affinity of intermolecular SPD-5 interactions such that they
399 become too strong and are unable to release and bind new molecules. Eventually, all
400 possible interaction motifs per SPD-5 molecule would be occupied, thus preventing the
401 addition of new molecules and capping growth. In theory, this would lead to high affinity
402 clusters of SPD-5 that are weakly connected to each other. Simulations of ideal

403 multivalent polymers demonstrated that this mechanism, termed “valency exhaustion”, is
404 sufficient to cause kinetic arrest and stop condensate growth (Ranganathan and
405 Shakhnovich, 2020). Consistent with this idea, we saw that PLK-1 phosphorylation initially
406 promoted SPD-5 assembly but then inhibited growth and prevented PCM condensate
407 fusion *in vitro* (Figure 1B,C). Alternatively, SPD-5 phosphorylation could create a new type
408 of interaction between SPD-5 molecules, which then leads to new material properties.
409 This is the case for amyloid formation in FUS condensates (Ranganathan and
410 Shakhnovich, 2022). Our microrheology showed that unphosphorylated PCM
411 condensates have one crossover between G' and G" at low frequency. In phosphorylated
412 PCM condensates, G' and G" cross over at even lower frequency, indicating an increase
413 in elastic character, but they also approach toward a second crossover point at higher
414 frequency. A second crossover would indicate that the condensate has acquired more
415 complex material properties, but what this means at the molecular level is still unclear
416 (Liu et al., 2006). Regardless of the finer mechanism, our results argue that
417 hyperphosphorylation increases intermolecular interactions between neighboring
418 molecules at the expense of less connectivity at the mesoscale, thus leading to defects
419 in overall PCM assembly and mechanical integrity.

420 The tunable viscoelastic nature of the PCM scaffold could help make sense of
421 previous conflicting results concerning PCM dynamics and architecture. For example, *C.*
422 *elegans* PCM is spherical and grows isotopically (Laos et al., 2015), which is expected
423 for a viscous liquid. On the other hand, in situ cryo-electron tomography showed that PCM
424 contains an underlying fibrous meshwork (Tollervey et al., 2025), which would be
425 expected for an elastic solid. One mystery arising from this work was that the pore size
426 of the meshwork was ~6-8 nm, which, if static, would be too small to accommodate large
427 PCM proteins and complexes (e.g., TPXL-1, ZYG-9, γ-tubulin ring complex) (Tollervey et
428 al., 2025). A viscoelastic PCM could achieve these complex features. Viscous behavior
429 over longer time scales would allow for rearrangements in the scaffold. This would allow
430 pore dilation needed accommodate larger proteins and movement of material to achieve
431 isotropic growth. Elastic behavior over longer time scales would maintain the overall
432 structure of the scaffold and allow it to resist microtubule pulling forces.

433 Recently, it was shown that PCM in *D. melanogaster* embryos is a composite of a
434 stable scaffold of Cnn proteins co-existing with a dynamic phase of TACC protein (Wong
435 et al., 2025). The Cnn scaffold seems to be important for mechanical strength (Lucas and
436 Raff, 2007), while the TACC scaffold is required to recruit specific clients (Wong et al.,
437 2025). This combination of static and dynamic scaffolds suggests that fly PCM is also
438 viscoelastic. Future work should use rheology to test if PCM from flies and other species
439 is similarly viscoelastic and regulated by phosphorylation. We speculate that tunable
440 viscoelasticity is a universal design principle for PCM across eukaryotes.
441

442 **ACKNOWLEDGEMENTS**

443 We thank Jessica Feldman for advice on performing embryo laser extrusion, Jordan Raff
444 for advice on *in vivo* experiments, and Anthony Hyman for antibodies.

445 **DATA AVAILABILITY**

446 Further requests and information for resources and reagents should be directed to and
447 will be fulfilled by the Lead Contact, Jeffrey Woodruff
448 (Jeffrey.woodruff@utsouthwestern.edu).

449 **COMPETING INTERESTS**

450 The authors declare no competing interests.

451 **FUNDING**

452 J.B.W. is supported by an R35 grant from the National Institute of General Medical
453 Sciences (1R35GM142522) and the Endowed Scholars program at UT Southwestern.
454 M.A. was supported by a National Research Service Award T32 (GM131963). Research
455 in the Rosen lab was supported by the Howard Hughes Medical Institute and grants
456 from the Welch Foundation (I-1544-20230405) and the National Institute of General
457 Medical Sciences (5R35GM141736).

458

459 **AUTHOR CONTRIBUTIONS**

460 M. Amato performed all experiments and analyzed data. J.H. Hwang performed the
461 microrheology experiments. M.U. Rios developed and optimized the embryo extrusion
462 assay and performed and analyzed extrusion experiments. N.E. Familiari made
463 baculoviruses and expressed proteins. J.B. Woodruff made transgenic *C. elegans* strains.
464 M. Amato and J.B. Woodruff wrote the manuscript. M.K. Rosen and J.B. Woodruff
465 supervised the project.

466

467 **MATERIALS AND METHODS**

468 **Experimental model and subject details**

469 For the expression of recombinant proteins (listed in Table S1), we used SF9-ESF *S.*
470 *frugiperda* insect cells grown at 27°C in ESF 921 Insect Cell Culture Medium (Expression
471 Systems) supplemented with Fetal Bovine Serum (2% final concentration). *C. elegans*
472 worm strains were grown on nematode growth media (NGM) plates at 23°C, following
473 standard protocols (www.wormbook.org). Worm strains used in this study are listed in
474 Table S2.

475 **Generation of transgenic *C. elegans***

476 *C. elegans* worm strains used in this study were created with MosSCI (Frokjaer-Jensen
477 et al., 2008) and are based on constructs made previously (Woodruff et al., 2015).
478 GFP::SPD-5(4E) mutant was created by replacing a section of the wild-type sequence
479 with a mutated gene block. All plasmids were purified using a NucleoBond Xtra Midi Prep
480 Kit (Macherey Nagel), combined with co-injection plasmids, and injected into strain
481 EG6699 (tt5605, Chr II). After one week, worms were heat-shocked for 3 hr at 35°C to kill
482 worms maintaining extrachromosomal arrays. Moving worms without fluorescent co-
483 injection markers were selected as candidates. Sequencing was used to confirm
484 transgene integration.

485 **Protein purification**

486 All expression plasmids are listed in Table S1. SPD-5, TPXL-1 and PLK-1 constructs were
487 expressed and purified as previously described (Woodruff et al., 2017; Woodruff and
488 Hyman, 2015; Woodruff et al., 2015). Baculoviruses were generated using the FlexiBAC
489 system (Lemaitre et al., 2019) in SF9 cells. Protein was harvested 72 hr after infection
490 during the P3 production phase. Cells were collected, washed, and resuspended in
491 harvest buffer (25 mM HEPES, pH 7.4, 150 mM NaCl). All subsequent steps were
492 performed at 4°C. Cell pellets were resuspended in buffer A (25 mM HEPES, pH 7.4, 30
493 mM imidazole, 500 mM KCl, 0.5 mM DTT, 1% glycerol, 0.1% CHAPS) + protease
494 inhibitors and then lysed using a dounce homogenizer. Proteins were bound to Ni-NTA
495 (Qiagen), washed with 10 column volumes of buffer A, and eluted with 250 mM imidazole.
496 For SPD-5 proteins, Ni-NTA eluate was then bound to MBP-Trap beads (Chromotek) and
497 washed with 5 column volumes of buffer A and eluted with by adding PreScission
498 protease, incubating overnight and then passing over Ni-NTA to remove the Precission
499 protease. For TPXL-1 proteins, Ni-NTA eluate was equilibrated with binding buffer (25 mM
500 HEPES, pH 7.4, 150 mM KCl) and then bound to SP Sepharose (GE Healthcare catalog
501 No: 10261262) and washed with 5 column volumes of binding buffer. TPXL-1 was eluted
502 using buffer A. For PLK-1 proteins, Ni-NTA eluate was concentrated with a 30 K MWCO
503 Amicon concentrator (Millipore), filtered, and then passed over a Superdex 75 increase
504 size exclusion column (Cytiva). Purified proteins were then concentrated using 30 K
505 MWCO Amicon concentrators (Millipore). All proteins were aliquoted in PCR tubes, flash-
506 frozen in liquid nitrogen, and stored at −80°C. Protein concentration was determined by
507 measuring absorbance at 280 nm using a NanoDrop ND-1000 spectrophotometer
508 (Thermo Fisher Scientific).

509 **RNAi treatment**

510 RNAi was done by feeding. RNAi feeding using *gpr-1/2*, *csnk-1*, feeding clones from the
511 Ahringer and Vidal collections (Source BioScience;(Rual et al., 2004)) The *spd-5* feeding
512 clone targets a region that is reencoded in our MosSCI transgenes (Woodruff et al., 2015).
513 Bacteria were seeded onto nematode growth media (NGM) supplemented with 1 mM
514 isopropyl β-D-1-thiogalactopyranoside (IPTG) and 100 µg/mL ampicillin. For
515 chromosome segregation experiments, *spd-5* feeding clone was combined with either

516 *csnk-1* or *gpr-1/2* feeding clone and plated as before. L4 hermaphrodites were grown on
517 feeding plates at 23°C for 24-34 hr or at 16°C for 24-34 hr in worms expressing *emb-*
518 *30(ts)*.

519 Target sequence for *spd-5(RNAi)*

520 5′-TGG AAT TGT CCG CTA CTG ATG CAA ACA ACA CAA CTG TCG GAT CTT TTC GTG
521 GAA CTC TTG ATG ACA TTC TGA AGA AAA ACG ATC CAG ATT TCA CAT TAA CCT
522 CTG GTT ATG AAG AAA GAA AGA TCA ACG ACC TGG AGG CAA AGC TCC TCT CTG
523 AGA TCG ACA AGG TAG CTG AGC TGG AAG ATC ACA TTC AGC AGC TCC GTC AAG
524 AAC TTG ACG ACC AAT CTG CAA GGC TTG CCG ATT CAG AAA ATG TTC GCG CTC
525 AGC TTG AAG CGG CCA CTG GAC AAG GAA TCC TCG GAG CTG CTG GAA ACG
526 CTA TGG TTC CAA ATT CAA CGT TCA TGA TCG GGA ACG GTC GTG AAT CAC AGA
527 CGC GAG ACC AGC TCA ATT ACA TTG ATG ATC TTG AAA CGA AGT TAG CTG ATG
528 CGA AGA AGG AAA ATG ATA AGG CTC GTC AGG CAC TCG TTG AAT ACA-3′.

529 **Western blotting**

530 45 adult worms were picked and transferred to blank plates for 20 min to remove bacteria
531 from their bodies. Worms were then moved to PCR tubes containing 10 µl of milli-Q water
532 to which 10 µl of SDS loading buffer was added. Samples were separated by SDS-PAGE.
533 Protein from each gel was transferred to a nitrocellulose membrane using a Trans-blot
534 turbo transfer for high molecular weight proteins (10 min). Membranes were incubated in
535 a blocking buffer consisting of TBS-T + 3% Blotting-Grade Blocker (BioRad) shaking at
536 room temperature for 1 hr. Membranes were then washed three times with TBS-T and
537 incubated shaking with primary antibodies overnight at 4°C. The primary antibody was
538 washed off three times with TBS-T and incubated with secondary antibodies at room
539 temperature for 1 hr. Each membrane was then incubated in ECL reagent (Thermo Fisher
540 Scientific SuperSignal West Femto) for 5 min and imaged with a ChemiDoc Touch
541 Imaging System. Primary antibodies: Mouse anti-alpha tubulin (Product No: 3873S;
542 1:1,000; Cell Signaling Technologies); Rabbit anti-SPD-5 C-terminus (1:1,000, clone 785,
543 Dresden Antibody Facility; Pelletier et al., 2004). Secondary Antibodies (1:50,000 for all):
544 HRP conjugated Goat anti-Rabbit IgG (1 mg/ml) (catalog No: 65-6120, catalog No:
545 J276300; Invitrogen); HRP conjugated Goat anti-Mouse (1.5 mg/ml) (Catalog No: 62-

546 6520, Catalog No: WA312227; Invitrogen); and HRP conjugated Donkey anti-Goat (1
547 mg/ml) (Catalog No: A15999, Catalog No: 58-155-072318; Invitrogen).

548 **Microscopy of *C. elegans* embryos**

549 Embryos from adult worms were dissected on a 22 × 22 mm coverslip (Catalog No: 2975-
550 225; Coring) using a 22-gauge needles in a 7 µl solution of egg salts buffer (ESB) (118mM
551 NaCl, 48mM KCl, 2mM $CaCl_2$, 2mM $MgCl_2$, 25mM Hepes) or M9 buffer. Samples were
552 then mounted onto plain 25 × 75 × 1 mm microscope slides (Catalog No: 12-544-4; Fisher
553 Scientific). Time-lapse images were acquired with an inverted Nikon Eclipse Ti2-E
554 microscope with a Yokogawa confocal scanner unit (CSU-W1), piezo Z stage, and an
555 iXon Ultra 888 EMCCD camera (Andor), controlled by Nikon Elements software. We used
556 a 100X Plan Apo silicon immersion objective (NA 1.35). To quantify GFP::SPD-5
557 transgene intensity we imaged at 15-18 × 1-µm Z-stacks using 488-nm at 2 x 2 binning,
558 15% laser power, 100 ms exposures every 20 seconds until centrosome disassembly
559 except where specified.

560 For microtubule depolymerization assays, one-cell embryos from adult worms were
561 treated with ESB mixed with nocodazole to make a 40 µM nocodazole solution or 2%
562 DMSO solution and imaged prior to PNM. For SPD-5 growth curves one-cell embryos
563 from adult worms were dissected in M9 and imaged prior to pronuclear meeting (PNM).

564 ***In vivo* FRAP of metaphase arrested embryos**

565 Metaphase arrest was achieved by temperature inactivation of *emb-30(ts)* by incubating
566 embryos from 16℃ to 25℃ for 15 minutes. One-cell embryos from adult worms were
567 dissected in M9 buffer and identified prior to metaphase. Metaphase arrest was
568 determined by chromosomes positioned at the metaphase plate. After 200 s post
569 metaphase arrest, stable PCM was imaged before photobleaching and every 20 s after
570 photobleaching for 140 s. PCM was photobleached with a 405-nm laser using a roi the
571 area of the centrosome at 20% intensity, 250 µs dwell time. Mean GFP::SPD-5 transgene
572 intensity was measured and normalized to the mean intensity of the centrosome prior to
573 photobleaching as the highest value and cytoplasmic region as the lowest value. To

574 validate PCM mass was stable during arrest, the mean GFP::SPD-5 transgene intensity
575 of the unbleached centrosome was recorded.

576 ***In vivo* partial FRAP of centrosomes**

577 One-cell embryos from adult worms were dissected in M9 buffer and photobleached with
578 a 405-nm laser at NEBD using a stim point positioned in the center of centrosomes at 1%
579 intensity, 50 ms dwell time. To quantify the intensity of GFP::SPD-5 transgene after
580 photobleaching a 5 μm line scan was positioned at centrosomes such that the maximum
581 and minimum intensity occurred at 1.82 μm and 2.6 μm respectively. GFP::SPD-5
582 transgene intensity was recorded immediately after photobleaching and 100 s thereafter.
583 Intensities are averaged over replicates and normalized to the maximum intensity
584 immediately after photobleaching.

585 **Centrosome extrusion assay**

586 Dissected one-cell embryos from adult worms were coated in a solution of 10 μm
587 Calcofluor-white (Biotium catalog No: 29067) in high salt buffer (150mM KCl, 25mM
588 Hepes pH 7.4). or MQ H20 with 25mM Hepes pH 7.4. In PP2A inhibition experiments,
589 centrosomes were extruded into high salt buffer containing 10 μM LB-100. To extrude
590 centrosomes, a 405 nm laser was targeted to the periphery of the eggshell using (100%
591 laser intensity, 500 ms dwell time). Cell cycle stage was determined by chromosome
592 organization via mCherry::H2B signal. Imaging was performed as above with a 60 × 1.2
593 NA Plan Apochromat water-immersion objective, GFP/mCherry splitter, 2 x 2 binning, 488
594 nm laser (15% intensity), 561 nm laser (10% intensity), 51 x 0.5 μm Z-steps, every 2 min
595 for 60 min or until centrosomes completely dissolved. The integrated density of
596 GFP::SPD-5 was normalized to centrosome intensity prior to extrusion in the normalized
597 plot.

598 High resolution imaging of GFP-SPD-5(4E) was performed using 100X Plan Apo silicon
599 immersion objective (NA 1.35) imaged at 15-18 × 1-μm Z-stacks using 488-nm at 2 x 2
600 binning, 15% laser power, 100 ms exposures every 5 s until centrosomes left the field of
601 view.

602 **Chromosome segregation defects**

603 To quantify chromosome segregation defects in embryos expressing *gfp::spd-5*
604 *transgenes* treated with various RNAi one-cell embryos were dissected into M9 and
605 imaged prior to metaphase until telophase. Chromosome segregation defects were
606 determined by organization of DNA visualized by mCherry::H2B signal. Embryos were
607 imaged at 15-18 × 1-µm Z-stacks using 488-nm at 2 x 2 binning, 15% laser power, 561-
608 nm at 2 x 2 binning, 20% laser power, 100 ms exposures every 20 seconds.

609

610 **96-well glass bottom passivation**

611 To clean a 96-well glass bottom imaging plate, wells were then treated with a solution of
612 5% v/v Hellmanex (Sigma-Aldrich catalog No: Z805939) for 1hr and washed 10X in H2O
613 and dried. A solution of 5M NaOH is added to wells for 1hr and washed 5X with H2O. To
614 passivate the surface of the wells, the 96-well glass-bottom imaging plate was treated
615 with a solution of 0.5% w/v of mPEG-Silane, MW 5,000 (Creative PEGWorks catalog No:
616 PLS-2011) in 95% EtOH for 1hr and then washed 10X with H2O and dried. On the day of
617 the experiment, a solution of 5% w/v of Bovine Serum Albumin (BSA) (Sigma-Aldrich)
618 was incubated in the wells for 30 min, washed 5X with H2O and then dried.

619

620 ***In vitro* PCM scaffold reconstitution and imaging**

621 To reconstitute PCM scaffold assembly from purified components we incubated 1µM
622 SPD-5::RFP, 1µM TPXL-1::GFP, 75mM KCl, 1mM DTT, 0.4mM ATP, 1mM $MgCl_2$,4mM
623 Hepes pH 7.4, except where indicated, in a passivated 96-well glass-bottom imaging plate
624 for 15 min. To prevent evaporation wells are covered with parafilm (Bemis). To image
625 reconstituted PCM we used at 100x silicon objective an inverted Nikon Eclipse Ti2-E
626 microscope with a Yokogawa confocal scanner unit (CSU-W1), piezo Z stage, and an
627 iXon Ultra 888 EMCCD camera (Andor), controlled by Nikon Elements software. Imaging
628 was performed at 488-nm; 2 x 2 binning, 1% intensity, 100ms exposure, and 561-nm; 1x1
629 binning, 5% intensity, 100ms exposure at a single imaging plane at the surface of the
630 glass except where specified. For condensate FRAP and fusion assays, we imaged at
631 0.5 x 10µm relative to the surface of the glass well.

632

633 ***In vitro* PCM scaffold FRAP assay**

634 To measure the dynamics of reconstituted PCM scaffolds, we incubated samples (as
635 above) with 0.5 μM PLK-1(CA) or 0.5 μM PLK-1(KD) for 30 minutes and then
636 photobleached with a 405 nm laser using a rectangular ROI positioned within
637 condensates at 20% intensity, 200 μs dwell time. We imaged condensates at 0.5 x 10 μm
638 relative to the surface of the glass well. The mean intensity of SPD-5::RFP and TPXL-
639 1::GFP was recorded prior to photobleaching and recorded every 15 seconds for 10 min
640 post photobleaching. Mean intensities were normalized to mean intensity prior to
641 photobleaching. 6 and 5 replicated were performed for PLK-1(KD) and PLK-1(CA)
642 conditions respectively.

643 ***In vitro* PCM scaffold dilution assay**

644 To determine the sensitivity to dilution of reconstituted PCM, we prepared reconstituted
645 PCM scaffolds using 1μM SPD-5::RFP, 1μM TPXL-1::GFP, 50mM KCl, 1mM DTT, 0.4mM
646 ATP, 1mM $MgCl_2$,4mM Hepes pH 7.4 and incubated with 0.5 μM PLK-1(CA) or 0.5 μM
647 PLK-1(KD) in a cleaned non-passivated 96-well glass imaging plate. Samples were
648 incubated for 1hr and Imaged. Samples were then diluted samples with 4.3x extrusion
649 buffer (150mM KCl, 25mM Hepes pH 7.4) and incubated for an additional hour and
650 imaged. We measured the total integrated density of SPD-5::RFP prior and after dilution
651 in which 6 images at different locations at the surface of the glass well were gathered for
652 each condition.

653 In the case of SPD-5(4E)::GFP, PCM condensates were prepared using 1μM SPD-
654 5(4E)::GFP, 1μM TPXL-1, 50mM KCl, 1mM DTT, 4mM Hepes pH 7.4 n a cleaned non-
655 passivated 96-well glass imaging plate. Samples were incubated and imaged as before
656 but instead diluted 4.3x into (250mM KCl, 25mM Hepes pH 7.4).

657

658 ***In vitro* PCM scaffold assembly assay**

659 To determine the effect of PLK-1 phosphorylation on the assembly of reconstituted PCM
660 scaffolds, we incubated 1μM SPD-5::GFP, 1μM TPXL-1, 50mM KCl, 1mM DTT, 0.4mM

661 ATP, 1mM $MgCl_2$, 4mM Hepes pH 7.4 with 0.5μM PLK-1(CA) or 0.5μM PLK-1(KD) in a
662 passivated 96-well imaging plate. We imaged using 488-nm; 2 x 2 binning, 1% intensity,
663 100ms exposure. 3 images at distinct locations at the surface of the glass well were
664 recorded at every interval for intervals 5, 10, 15, 20, 30, 45, 60, 90 minutes from one
665 experiment for PLK-1(CA) and PLK-1(KD). Condensate size was measured using a semi-
666 automated threshold-based analysis. The watershed function in FIJI was used to
667 segregated chains of condensates.
668

669 **Video particle tracking microrheology sample preparation**

670 Samples were prepared in 384-well glass bottom microwell plates (Brooks Life Science
671 Systems: MGB101-1-2-LK-L). Prior to use, the plates were cleaned with 5% Hellmanex
672 III (Hëlma Analytics), etched with 1M KOH, and siliconized with Sigmacote (Sigma-
673 Aldrich). On the day of the experiment, individual wells were blocked with 1% bovine
674 serum albumin, then rinsed thoroughly with MilliQ-water. PCM samples were prepared
675 with 1 μM SPD-5::GFP, 1 μM TPXL-1, 50 mM KCl, 0.4 mM ATP, 1 mM $MgCl_2$,1mM Hepes
676 pH 7.4 pH), 150 beads/μL with 0.2 μM PLK-1(KD) or 0.2 μM PLK-1(CA) and 100 nm-
677 diameter carboxylate-modified fluorescent beads (Invitrogen: F8801). The final
678 concentration of beads was <150 beads/μL. Samples were incubated inside the
679 temperature-controlled microscope chamber at 30°C for at least 1 hour before imaging.

680 **Video particle tracking microrheology microscopy**

681 Images were captured on a Lecia DMI6000 B microscope base with a Yokogawa CSU-
682 X1 spinning disk confocal scanner unit and a 405/488/561/647 nm Laser Quad Band Set
683 filter cube (Chroma) with a plan apo 63 or 100 × 1.40 NA oil immersion objective. Images
684 were acquired using a Hamamatsu ImagEMX2 EM-CCD camera at 15ms/frame using
685 stream acquisition function on Metamorph (Biovision) software. At least 10000 frames (3-
686 25 min) were acquired for each acquisition, up to 6 acquisitions were made per sample
687 per session, and at least 3 sessions were carried out per sample for reproducibility.

688 **Video particle tracking microrheology data analysis**

Particle tracking and calculation of mean squared displacement (MSD) was performed using MATLAB codes by Daniel Blair & Eric Dufresne (https://site.physics.georgetown.edu/matlab/code.html). Average MSD was calculated from >17000 individual trajectories and smoothed using a moving average with span <10% of total number of frames. Elastic (G') and viscous (G") moduli as a function of frequency (ω) were calculated from the averaged MSD from 0.015 to 100s using generalized Stokes-Einstein relation (GSER) as described by Mason TG (Rheologica Acta, 2000) using MATLAB codes by Andrew Sun (https://github.com/andrewx101/track_analysis/releases/tag/v2.05). Viscosity (η) is calculated (η = G"/ω) and plotted against frequency. From viscosity plot, the mean value of the plateau at the low frequency was used to estimate the zero-shear viscosity (η_0).

Image quantification and statistical analysis

Images were analyzed using a semiautomated, threshold-based particle analysis in FIJI (https://fiji.sc/). MATLAB (Mathworks) was used to analyze VPT experiments. All data are expressed as the mean ± 95% confidence intervals as stated in the figure legends and results. The value of n and what n represents (e.g., number of centrosomes, condensates or experimental replicates) is stated in figure legends and results. A Brown-Forsythe and Welch ANOVA statistical test were used for normally distributed data, and a Kruskal-Walis were used for non-normally distributed data. Significance was reported as; p value < 0.05 = *, p value < 0.005 = **, p value < 0.0005 = ***, p value of < 0.00005 = ****.

TABLE S1. Baculoviral expression constructs for protein expression.

protein	sequence	plasmid name	parent plasmid (pOCC #)	N-term tag	C-term tag	species
SPD-5	Full-length	JWV1	pOCC28	MBP-PreScission	eGFP-PreScission-6xHis	*C.elegans*

SPD-5	Full-length	JWV3	pOCC25	MBP-PreScission	RFP-PreScission-6xHis	*C.elegans*
SPD-5	Full-length	JWV10	pOCC27	MBP-PreScission	eGFP-PreScission-6xHis	*C.elegans*
TPXL-1	Full-length	JWV29	pOCC27	MBP-PreScission	eGFP-PreScission-6xHis	*C.elegans*
TPXL-1	Full-length	JWV30	pOCC28	MBP-PreScission	PreScission-6xHis	*C.elegans*
PLK-1(CA)	Full-length T194D	JWV11	pOCC7	6xHis-Prescission	-	*C.elegans*
PLK-1(KD)	Full-length K67M	JWV12	pOCC7	6xHis-Prescission	-	*C.elegans*

711

712

713 **TABLE S2. C. elegans strains.**

Strain name	genotype	Creation method	Origin
JWW12	unc-119(ed9) III; ltSi202[pVV103/ pOD1021; Pspd-2::GFP::SPD-5 RNAiresistant;cb-unc-119(+)]II	MosSCI into EG6699	(Woodruff et al., 2015)
JWW69	unc-119(ed9) III; ltSi202[pVV103/ pOD1021; Pspd-2::GFP::SPD-5 re-encoded;cb-unc-119(+)]II; ltIs37 [(pAA64) pie-1p::mCherry::his-58 + unc-119(+)] IV.	MosSCI into EG6699	This study

JWW70	unc-119(ed9) III; utsw1[pJWB56; Pspd-2::GFP::SPD-5(530E, 627E, 653E, 658E) re-encoded; cb-unc-119(+)]II; ltIs37 [(pAA64) pie-1p::mCherry::his-58 + unc-119(+)] IV.	MosSCI into EG6699	This study
JWW254	mCherry::his-58, unc-119(ed9) III; ltSi228[pVV153/ pOD1615; Pspd-2::GFP::spd-5 S530A,S627A, S653A, S658A reencoded; cb-unc-119(+)]II	MosSCI into EG6699	(Woodruff et al., 2015)
DG627	emb-30(tn377) III.	EMS mutagenized	(Furuta et al., 2000)
JWW155	emb-30(tn377) III; ltSi202[pVV103/ pOD1021; Pspd-2::GFP::SPD-5 re-encoded;cb-unc-119(+)]II; ltIs37 [(pAA64) pie-1p::mCherry::his-58 + unc-119(+)] IV.	Cross of JWW69 with DG627	This study
JWW243	emb-30(tn377) III. unc-119(ed9) III; utsw1[pJWB56; Pspd-2::GFP::SPD-5(530E, 627E, 653E, 658E) re-encoded; cb-unc-119(+)]II; ltIs37 [(pAA64)	Cross of JWW70 with DG627	This study
JWW266	emb-30(tn377) III. unc-119(ed9) III; utsw1[pJWB56; Pspd-2::GFP::SPD-5(530A, 627A, 653A, 658A) re-encoded; cb-unc-119(+)]II; ltIs37 [(pAA64)	Cross of JWW254 with DG627	This study

FIGURE LEGENDS

Figure 1: PLK-1 phosphorylation changes the dynamics and material properties of reconstituted PCM scaffolds.

a. Reconstitution of PCM condensates using purified SPD-5, TPXL-1, and no molecular crowding agent. Proteins were assembled for 15 min in buffer (75 mM KCl, 4 mM Hepes pH 7.4, 10 mM DTT, 0.4 mM ATP, 1 mM $MgCl_2$) and imaged in a 96-well glass bottom plate using confocal fluorescence microscopy.

724 b. *In vitro* PCM condensate assembly assay over time. Top, representative images.
725 Bottom, quantification of average condensate size over time (mean +/- 95% C.I.;
726 n>100 condensates from 3 replicates).
727 c. Samples were prepared as in (A) with 0.5 μM kinase dead PLK-1(KD) or
728 constitutively active PLK-1(CA) and imaged after 30 min. Top panel, static images.
729 Bottom panel, timelapse imaging of condensates. Arrows indicate the site of
730 condensate fusion.
731 d. Fluorescence recovery after photobleaching of SPD-5/TPXL-1 condensates. Top,
732 SPD-5::RFP intensity was measured and normalized (mean +/- 95% C.I.; PLK-
733 1(KD) n = 6, PLK-1(CA) n = 6 condensates). Bottom, images of bleached
734 condensates.
735 e. Dilution assay of reconstituted PCM. 1 μM SPD-5::RFP, 1 μM TPXL-1::GFP was
736 incubated in buffer (50 mM KCl, 4 mM Hepes pH 7.4, 10 mM DTT, 0.4 mM ATP, 1
737 mM $MgCl_2$) with 0.5 μM PLK-1 (KD) or 0.5 μM PLK-1(CA) for 1 hr and imaged.
738 Samples were then diluted 4.3X into extrusion buffer (150mM KCl, 25mM Hepes
739 pH.7.4) and imaged after 1 hr (left panels). Right, quantification of SPD-5::RFP
740 integrated density before and after dilution (mean +/- 95% C.I.; PLK-1(KD) n=6
741 images, PLK-1 (CA) n=6 images with >100 condensates).
742
743 **Figure 2: Phosphorylation increases the viscoelasticity of reconstituted PCM**
744 **scaffolds.**

745 a. Schematic of Video Particle Tracking (VPT) technique. 100 nm-diameter
746 carboxylate-modified fluorescent beads were encapsulated in reconstituted PCM
747 condensates. Left, representative spinning-disc confocal fluorescence image. Top
748 right, diagram of condensate with bead; not to scale. Bottom right, representative
749 trajectory of a single bead within a condensate.
750 b. Plot for averaged mean squared displacement (MSD) of beads encapsulated in
751 reconstituted PCM condensates incubated with 0.2 μM PLK-1(KD) or PLK-1(CA).
752 c. Viscoelastic moduli of condensates determined from VPT. Moduli were calculated
753 using the generalized Stokes-Einstein relation fit to a maxwell fluid from the
754 averaged MSD from 0.015 to 100 s. For G' and G", solid lines indicate measured

755 values, dashed lines indicate extrapolated values. Dashed grey line indicates
756 crossover frequency.
757 d. Viscosity was calculated from averaged MSD from 0.015 to 100 s. The mean value
758 of the plateau at the low frequency was used to estimate the zero-shear viscosity
759 (η_0). Solid lines indicate measured values, dashed lines indicate extrapolated
760 values.
761 e. Summary of in vitro rheological and dynamics measurements.
762
763 **Figure 3: The phosphorylation state of SPD-5 affects its dynamics in metaphase-**
764 **arrested embryos.**
765 a. Top, diagram of key PLK-1 phosphorylation sites in SPD-5. Bottom, design of
766 *gfp::spd-5* transgenes expressed at the Mos locus on chromosome II.
767 b. Top, representative image of metaphase arrest in one-cell *emb-30(ts)* embryos
768 expressing GFP::SPD-5(WT) and mCherry::H2B. Right, characterization of
769 PCM size during metaphase arrest. Bottom, normalized integrated density of
770 GFP::SPD-5 200-340 s after metaphase arrest (mean +/- 95% C.I.; n= 12
771 embryos).
772 c. Representative images for fluorescence recovery after photobleaching (FRAP)
773 of PCM in metaphase-arrested embryos. PCM was photobleached at 200 s
774 post metaphase arrest in one-cell embryos expressing *gfp::spd-5* transgenes
775 with and without RNAi against endogenous *spd-5*.
776 d. Quantification of (C). GFP mean intensity was measured every 20 s until 140
777 s and normalized (mean +/- 95% C.I.; GFP::SPD-5(WT) n= 12, GFP::SPD-
778 5(WT) + *spd-5(RNAi) n= 7,* GFP::SPD-5(4E) n=8, GFP::SPD-5(4E) + *spd-*
779 *5(RNAi)* n=11, GFP::SPD-5(4A) n=9, GFP::SPD-5(4A) + *spd-5(RNAi)* n=7
780 centrosomes). Curves are fit to a one-phase nonlinear regression model.
781
782 **Figure 4: SPD-5 dynamics change with the cell cycle.**
783 a. Diagram of centrosome release and dilution via extrusion. *C. elegans* embryos
784 were coated with calcofluor white and eggshells were ruptured with a 405 nm laser.

785 b. Representative images of centrosomes (labeled with GFP::SPD-5) extruded from
786 a one-cell embryo at metaphase into low salt buffer (0mM KCl, 25mM HEPES pH
787 7.4). DNA is labeled with H2B::mCherry.
788 c. Representative images of centrosomes extruded from one-cell embryos in different
789 cell cycle stages into high salt buffer (150mM KCl, 25mM HEPES pH 7.4).
790 d. Quantification of integrated density of GFP::SPD-5 of extruded centrosomes
791 imaged every 2 minutes for 1 hr (mean +/- 95% C.I.; interphase n=11, metaphase
792 n=12, anaphase n=9 centrosomes).
793 e. Normalized data from D.
794 f. Normalized GFP integrated density of extruded centrosomes from metaphase
795 embryos expressing *gfp::spd-5 transgenes* with and without *spd-5(RNAi)*(mean +/-
796 95% C.I.; GFP::SPD-5(WT) n= 12, GFP::SPD-5(4E) n=5, GFP::SPD-5(4E) + *spd-*
797 *5(RNAi)* n=8, GFP::SPD-5(4A) n=9, GFP::SPD-5(4A) + *spd-5(RNAi)* n=10
798 centrosomes).
799 g. Representative images of extruded centrosomes in one-cell metaphase embryos
800 expressing *gfp::spd-5(4E)* treated with *spd-5(RNAi)* into low salt buffer (0mM KCl,
801 25mM Hepes pH 7.4).
802
803 **Figure 5: The phosphorylation state of SPD-5 is tuned to maximize the mechanical**
804 **integrity of the PCM.**
805 a. Transgenic worms were treated with *spd-5* RNAi to deplete endogenous SPD-5.
806 Left, one-cell embryos expressing *gfp::spd-5 transgenes* treated with 2% DMSO
807 or 40 μM nocodazole and imaged at nuclear envelope breakdown.
808 b. Quantification GFP integrated density at PCM (mean +/- 95% C.I.; WT + DMSO n
809 = 14, WT+ nocodazole n=10, 4E + DMSO n=18, 4E + nocodazole n=16, 4A +
810 DMSO n=20, 4A + nocodazole n=20; p values from Brown-Forsythe and Welch
811 ANOVA tests, followed by a Dunnet's multiple comparisons test).
812
813 **Figure 6: Proper SPD-5 phosphorylation is important for the fidelity of chromosome**
814 **segregation.**

a. Representative images of chromosome segregation in one-cell embryos expressing *gfp::spd-5 transgenes* treated with *spd-5(RNAi)* to deplete endogenous SPD-5, imaged from metaphase until telophase. DNA is visualized with H2B::mCherry.
b. Examples of chromosome segregation defects observed in (A).
c. Chromosome segregation in transgenic *spd-5(RNAi)* embryos combined with *csnk-1(RNAi)* to increase microtubule pulling forces (Left) or *gpr-1/2(RNAi)* to reduce microtubule pulling forces (Right).
d. Quantification of chromosome segregation defects in (A) and (C) reported as Percentage of embryos with chromosome segregation defects in (A) and (C). (gray panel: n= 29,29,23 (WT,4E,4A) embryos across 4 biological replicates; orange panel: n=20,17 (WT,4E) across 3 biological replicates; blue panel: (WT n=15 (WT,4A) across 3 biological replicates).

Figure 7: Phosphorylation tunes the functionally important viscoelastic properties of the PCM. Diagram of PCM architecture in a *C. elegans* embryo. Properly tuned PCM dynamics and viscoelasticity ensures PCM reaches full size and strength needed for function. Left, under-phosphorylated SPD-5 (orange) builds PCM that is too dynamic and weak, leading to a liquid-like PCM that gets quickly pulled apart by microtubule pulling forces. Right, over-phosphorylated SPD-5 (red) builds PCM that lacks dynamic character leading to solid-like PCM that is irregularly shaped and lacks mechanical integrity.

838 **SUPPLEMENTAL FIGURE LEGENDS**

839

840 **Figure S1. In vitro analysis of PCM.**

841 a. Coomassie gel of proteins used in this study.

842 b. Reconstituted PCM condensates. Representative images of reconstituted PCM
843 condensates prepared with 1 μM SPD-5::RFP, 1 μM TPXL-1::GFP, 50 mM KCl,
844 Hepes pH 7.4 and incubated for 15 min.

845 c. Representative images of reconstituted PCM condensates prepared with either 1
846 μM SPD-5:GFP(WT) or 1 μM SPD-5(4E), 1 μM TPXL-1::GFP, 50 mM KCl, Hepes
847 pH 7.4 and incubated for 30 min.

848 d. Dilution assay of reconstituted PCM. 1 μM SPD-5::GFP(WT) or 1 μM SPD-
849 5::GFP(4E), 1 μM TPXL-1::GFP was incubated in buffer (50 mM KCl, 4 mM Hepes
850 pH 7.4, 10 mM DTT, 0.4 mM ATP, 1 mM $MgCl_2$) with 0.5 μM PLK-1 (KD) or 0.5 μM
851 PLK-1(CA) for 1 hr and imaged. Samples were then diluted 4.3X into buffer
852 (200mM KCl, 25mM Hepes pH.7.4) and imaged after 1 hr (left panels). Right,
853 quantification of SPD-5::RFP integrated density before and after dilution (mean +/-
854 95% C.I.; PLK-1(KD) n=6 images, PLK-1 (CA) n=6 images with >100
855 condensates).

856 e. Fluorescence recovery after photobleaching (FRAP) of reconstituted PCM
857 condensates incubated with 0.5 μM PLK-1(KD) or 0.5 μM PLK-1(CA) for 30 min.
858 TPXL-1::GFP intensity was measured and normalized (mean +/- 95% C.I.; KD, n
859 = 5, CA n = 6 condensates).

860

861 **Figure S2. Effect of PP2A inhibition of PP2A on SPD-5 persistence in extruded PCM.**
862 Quantification of PCM from metaphase embryos expressing GFP::SPD-5(WT) +
863 endogenous SPD-5 extruded into high salt buffer (150mM KCl, 25mM Hepes pH 7.4)
864 (black curve), or high salt buffer with 10 μM LB-100 (green curve)(mean +/- 95% C.I.; no
865 drug n= 12, 10 μM LB-100 n=7 centrosomes).

866

867 **Figure S3. *In vivo* characterization of SPD-5(4E).**

868 a. PCM assembly in one-cell embryos expressing GFP::SPD-5 transgenes. Top left,
869 representative images taken at nuclear envelope breakdown (NEBD). Bottom left,
870 quantification of GFP::SPD-5 integrated density relative to NEBD. Top right, worms
871 were treated with RNAi to deplete endogenous SPD-5 (mean +/- 95% C.I.; WT
872 n=22, 4E n=22, WT + *spd-5(RNAi)* n=18, 4E + *spd-5(RNAi)* n=30).
873 b. Western blot against SPD-5. Alpha tubulin was detected as a loading control.
874 c. Time from pronuclear meeting (PNM) to nuclear envelope breakdown (NEBD) was
875 measured in one-cell embryos expressing GFP::SPD-5 transgenes (mean +/- 95%
876 C.I., p values from Kruskal-Wallis test followed by Dunn's multiple comparisons
877 test).
878
879 **Figure S4. Characterization of chromosome segregation defects in embryos**
880 **expressing *gfp::spd-5 transgenes*.**
881 a. Quantification of chromosome segregation defects by category in Figure 6A
882 and C (see figure 6D for n values).
883 b. Representative images of chromosome segregation defect categories.
884 Unfocused spindle poles were observed in cases where centrosomes broke
885 symmetry along the spindle axis.
886 c. Embryo viability assay (mean +/- 95% C.I.; WT n=8, WT + *spd-5(RNAi)* n=8,
887 4E n=7, 4E + *spd-5(RNAi)* n=8 mothers, >20 embryos counted per mother; p
888 values from a Kruskal-Wallis test followed by Dunn's multiple comparisons
889 test).
890
891 **Figure S5. Partial FRAP of PCM in embryos expressing *gfp::spd-5* transgenes**
892 **during mitosis.**
893 a. Top, diagram of key PLK-1 phosphorylation sites in SPD-5. Bottom, design of
894 *gfp::spd-5* transgenes expressed at the Mos locus on chromosome II. GFP::SPD-
895 5(2A) harbors two of the four S-to-A mutations present in GFP::SPD-5(4A).
896 b. Partial fluorescence recovery after photobleaching (FRAP) of PCM at nuclear
897 envelop breakdown in one-cell embryos (no RNAi). GFP intensity was measured
898 with a 5 μm line scan 0 s and 100 s after photobleaching (mean +/- 95% C.I.;

GFP::SPD-5(WT) n=16, GFP::SPD-5(4A) n=7, GFP::SPD-5(2A) n=8 centrosomes).

REFERENCES

Alshareedah, I., A. Singh, S. Yang, V. Ramachandran, A. Quinn, D.A. Potoyan, and P.R. Banerjee. 2024. Determinants of viscoelasticity and flow activation energy in biomolecular condensates. *Sci Adv*. 10:eadi6539.

Andre, A.A.M., N.A. Yewdall, and E. Spruijt. 2023. Crowding-induced phase separation and gelling by co-condensation of PEG in NPM1-rRNA condensates. *Biophys J*. 122:397-407.

Banani, S.F., H.O. Lee, A.A. Hyman, and M.K. Rosen. 2017. Biomolecular condensates: organizers of cellular biochemistry. *Nat Rev Mol Cell Biol*. 18:285-298.

Cohen, R., J. & Benedek, G. B. 1982. Equilibrium and kinetic theory of polymerization and the sol-gel transition. *J. Phys. Chem*. 86:3696–3714.

Colombo, K., S.W. Grill, R.J. Kimple, F.S. Willard, D.P. Siderovski, and P. Gonczy. 2003. Translation of polarity cues into asymmetric spindle positioning in Caenorhabditis elegans embryos. *Science*. 300:1957-1961.

Conduit, P.T., Z. Feng, J.H. Richens, J. Baumbach, A. Wainman, S.D. Bakshi, J. Dobbelaere, S. Johnson, S.M. Lea, and J.W. Raff. 2014. The centrosome-specific phosphorylation of Cnn by Polo/Plk1 drives Cnn scaffold assembly and centrosome maturation. *Dev Cell*. 28:659-669.

Decker, M., S. Jaensch, A. Pozniakovsky, A. Zinke, K.F. O'Connell, W. Zachariae, E. Myers, and A.A. Hyman. 2011. Limiting amounts of centrosome material set centrosome size in C. elegans embryos. *Curr Biol*. 21:1259-1267.

Enos, S.J., M. Dressler, B.F. Gomes, A.A. Hyman, and J.B. Woodruff. 2018. Phosphatase PP2A and microtubule-mediated pulling forces disassemble centrosomes during mitotic exit. *Biol Open*. 7.

Feng, Z., A. Caballe, A. Wainman, S. Johnson, A.F.M. Haensele, M.A. Cottee, P.T. Conduit, S.M. Lea, and J.W. Raff. 2017. Structural Basis for Mitotic Centrosome Assembly in Flies. *Cell*. 169:1078-1089 e1013.

Ferry, J.D. 1980. Viscoelastic Properties of Polymers. John Wiley & Sons, Inc, New York, NY.

Flory, P.J. 1953. Principles of Polymer Chemistry. Cornell University Press.

Flynn, J.R., and F.J. McNally. 2017. A casein kinase 1 prevents expulsion of the oocyte meiotic spindle into a polar body by regulating cortical contractility. *Mol Biol Cell*. 28:2410-2419.

Furuta, T., S. Tuck, J. Kirchner, B. Koch, R. Auty, R. Kitagawa, A.M. Rose, and D. Greenstein. 2000. EMB-30: an APC4 homologue required for metaphase-to-anaphase transitions during meiosis and mitosis in Caenorhabditis elegans. *Mol Biol Cell*. 11:1401-1419.

Golsteyn, R.M., K.E. Mundt, A.M. Fry, and E.A. Nigg. 1995. Cell cycle regulation of the activity and subcellular localization of Plk1, a human protein kinase implicated in mitotic spindle function. *J Cell Biol*. 129:1617-1628.

940 Gomes Pereira, S., M.A. Dias Louro, and M. Bettencourt-Dias. 2021. Biophysical and Quantitative
941 Principles of Centrosome Biogenesis and Structure. *Annu Rev Cell Dev Biol*. 37:43-63.
942 Hamill, D.R., A.F. Severson, J.C. Carter, and B. Bowerman. 2002. Centrosome maturation and
943 mitotic spindle assembly in C. elegans require SPD-5, a protein with multiple coiled-coil
944 domains. *Dev Cell*. 3:673-684.
945 Haren, L., T. Stearns, and J. Luders. 2009. Plk1-dependent recruitment of gamma-tubulin
946 complexes to mitotic centrosomes involves multiple PCM components. *PLoS One*.
947 4:e5976.
948 Harmon, T.S., A.S. Holehouse, M.K. Rosen, and R.V. Pappu. 2017. Intrinsically disordered linkers
949 determine the interplay between phase separation and gelation in multivalent proteins.
950 *Elife*. 6.
951 Kaur, T., I. Alshareedah, W. Wang, J. Ngo, M.M. Moosa, and P.R. Banerjee. 2019. Molecular
952 Crowding Tunes Material States of Ribonucleoprotein Condensates. *Biomolecules*. 9.
953 Laan, L., N. Pavin, J. Husson, G. Romet-Lemonne, M. van Duijn, M.P. Lopez, R.D. Vale, F. Julicher,
954 S.L. Reck-Peterson, and M. Dogterom. 2012. Cortical dynein controls microtubule
955 dynamics to generate pulling forces that position microtubule asters. *Cell*. 148:502-514.
956 Laos, T., G. Cabral, and A. Dammermann. 2015. Isotropic incorporation of SPD-5 underlies
957 centrosome assembly in C. elegans. *Curr Biol*. 25:R648-649.
958 Lee, K., and K. Rhee. 2011. PLK1 phosphorylation of pericentrin initiates centrosome maturation
959 at the onset of mitosis. *J Cell Biol*. 195:1093-1101.
960 Linsenmeier, M., M. Hondele, F. Grigolato, E. Secchi, K. Weis, and P. Arosio. 2022. Dynamic arrest
961 and aging of biomolecular condensates are modulated by low-complexity domains, RNA
962 and biochemical activity. *Nat Commun*. 13:3030.
963 Liu, C.Y., J.S. He, E. van Ruymbeke, R. Keunings, and C. Bailly. 2006. Evaluation of different methods
964 for the determination of the plateau modulus and the entanglement molecular weight.
965 *Polymer*. 47:4461-4479.
966 Lucas, E.P., and J.W. Raff. 2007. Maintaining the proper connection between the centrioles and
967 the pericentriolar matrix requires Drosophila centrosomin. *J Cell Biol*. 178:725-732.
968 Lyon, A.S., W.B. Peeples, and M.K. Rosen. 2021. A framework for understanding the functions of
969 biomolecular condensates across scales. *Nat Rev Mol Cell Biol*. 22:215-235.
970 Magescas, J., J.C. Zonka, and J.L. Feldman. 2019. A two-step mechanism for the inactivation of
971 microtubule organizing center function at the centrosome. *Elife*. 8.
972 Maiato, H., and E. Logarinho. 2014. Mitotic spindle multipolarity without centrosome
973 amplification. *Nat Cell Biol*. 16:386-394.
974 Megraw, T.L., K. Li, L.R. Kao, and T.C. Kaufman. 1999. The centrosomin protein is required for
975 centrosome assembly and function during cleavage in Drosophila. *Development*.
976 126:2829-2839.
977 Mittasch, M., V.M. Tran, M.U. Rios, A.W. Fritsch, S.J. Enos, B. Ferreira Gomes, A. Bond, M. Kreysing,
978 and J.B. Woodruff. 2020. Regulated changes in material properties underlie centrosome
979 disassembly during mitotic exit. *J Cell Biol*. 219.
980 Ohta, M., Z. Zhao, D. Wu, S. Wang, J.L. Harrison, J.S. Gomez-Cavazos, A. Desai, and K.F. Oegema.
981 2021. Polo-like kinase 1 independently controls microtubule-nucleating capacity and size
982 of the centrosome. *J Cell Biol*. 220.

983 Oshimori, N., M. Ohsugi, and T. Yamamoto. 2006. The Plk1 target Kizuna stabilizes mitotic
984 centrosomes to ensure spindle bipolarity. *Nat Cell Biol*. 8:1095-1101.
985 Panbianco, C., D. Weinkove, E. Zanin, D. Jones, N. Divecha, M. Gotta, and J. Ahringer. 2008. A
986 casein kinase 1 and PAR proteins regulate asymmetry of a PIP(2) synthesis enzyme for
987 asymmetric spindle positioning. *Dev Cell*. 15:198-208.
988 Ranganathan, S., and E. Shakhnovich. 2022. The physics of liquid-to-solid transitions in multi-
989 domain protein condensates. *Biophys J*. 121:2751-2766.
990 Ranganathan, S., and E.I. Shakhnovich. 2020. Dynamic metastable long-living droplets formed by
991 sticker-spacer proteins. *Elife*. 9.
992 Rios, M.U., M.A. Bagnucka, B.D. Ryder, B. Ferreira Gomes, N.E. Familiari, K. Yaguchi, M. Amato,
993 W.E. Stachera, L.A. Joachimiak, and J.B. Woodruff. 2024. Multivalent coiled-coil
994 interactions enable full-scale centrosome assembly and strength. *J Cell Biol*. 223.
995 Rios, M.U., W.E. Stachera, N.E. Familiari, C. Brito, T. Surrey, and J.B. Woodruff. 2025. In vitro
996 reconstitution of minimal human centrosomes. *bioRxiv*.
997 Rual, J.F., J. Ceron, J. Koreth, T. Hao, A.S. Nicot, T. Hirozane-Kishikawa, J. Vandenhaute, S.H. Orkin,
998 D.E. Hill, S. van den Heuvel, and M. Vidal. 2004. Toward improving Caenorhabditis elegans
999 phenome mapping with an ORFeome-based RNAi library. *Genome Res*. 14:2162-2168.
1000 Tollervey, F., M.U. Rios, E. Zagoriy, J.B. Woodruff, and J. Mahamid. 2025. Molecular architectures
1001 of centrosomes in C. elegans embryos visualized by cryo-electron tomography. *Dev Cell*.
1002 60:885-900 e885.
1003 Wong, S.S., J.M. Monteiro, C.C. Chang, M. Peng, N. Mohamad, T.L. Steinacker, B. Xiao, S. Saurya,
1004 A. Wainman, and J.W. Raff. 2025. Centrioles generate two scaffolds with distinct
1005 biophysical properties to build mitotic centrosomes. *Sci Adv*. 11:eadq9549.
1006 Woodruff, J.B., B. Ferreira Gomes, P.O. Widlund, J. Mahamid, A. Honigmann, and A.A. Hyman.
1007 2017. The Centrosome Is a Selective Condensate that Nucleates Microtubules by
1008 Concentrating Tubulin. *Cell*. 169:1066-1077 e1010.
1009 Woodruff, J.B., O. Wueseke, and A.A. Hyman. 2014. Pericentriolar material structure and
1010 dynamics. *Philos Trans R Soc Lond B Biol Sci*. 369.
1011 Woodruff, J.B., O. Wueseke, V. Viscardi, J. Mahamid, S.D. Ochoa, J. Bunkenborg, P.O. Widlund, A.
1012 Pozniakovsky, E. Zanin, S. Bahmanyar, A. Zinke, S.H. Hong, M. Decker, W. Baumeister, J.S.
1013 Andersen, K. Oegema, and A.A. Hyman. 2015. Centrosomes. Regulated assembly of a
1014 supramolecular centrosome scaffold in vitro. *Science*. 348:808-812.
1015 Wueseke, O., D. Zwicker, A. Schwager, Y.L. Wong, K. Oegema, F. Julicher, A.A. Hyman, and J.B.
1016 Woodruff. 2016. Polo-like kinase phosphorylation determines Caenorhabditis elegans
1017 centrosome size and density by biasing SPD-5 toward an assembly-competent
1018 conformation. *Biol Open*. 5:1431-1440.

1019

Figure 1

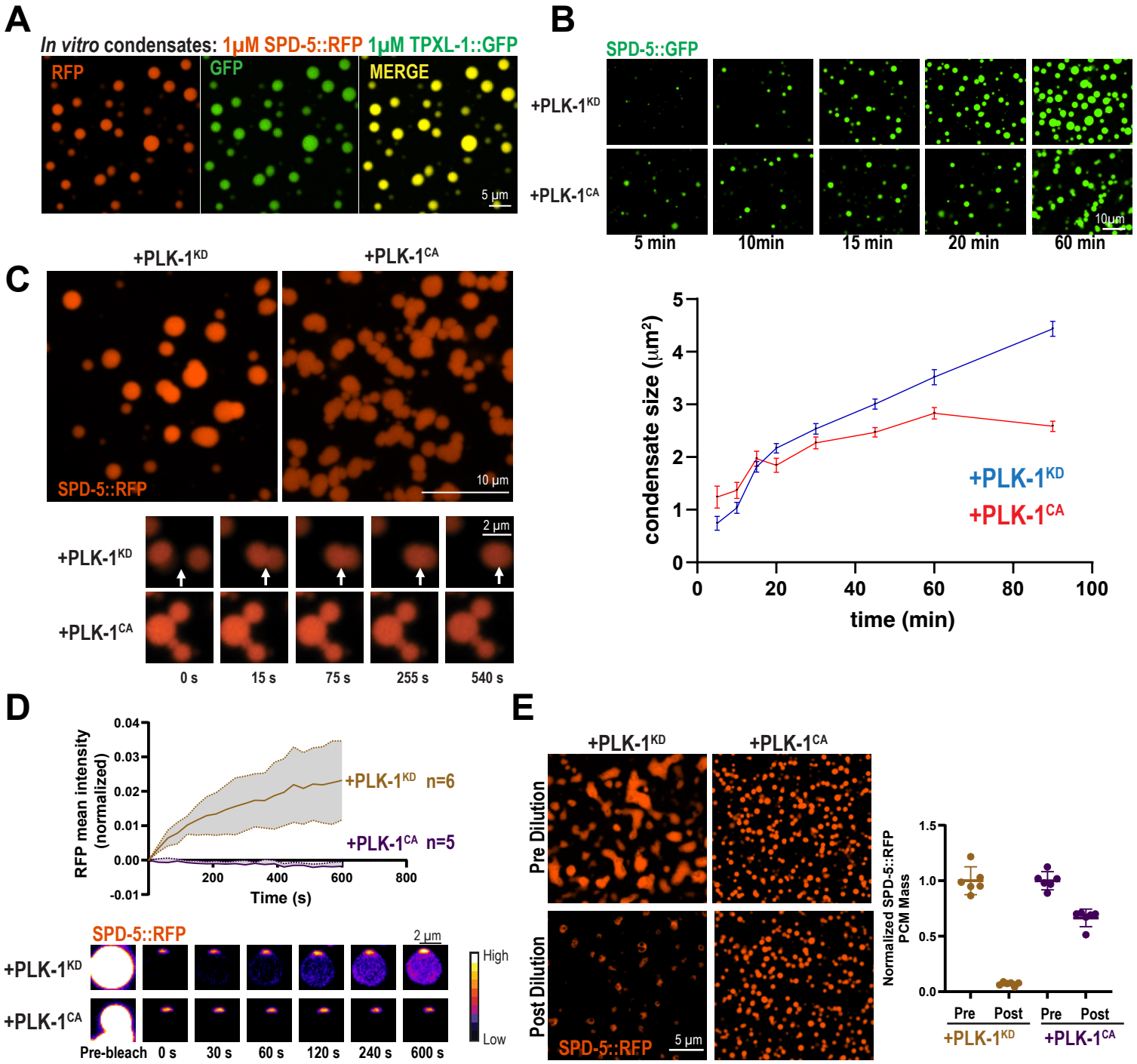
A
In vitro condensates: 1μM SPD-5::RFP 1μM TPXL-1::GFP
RFP
GFP
MERGE
5 μm
B
SPD-5::GFP
+PLK-1KD
+PLK-1CA
10μm
5 min
10min
15 min
20 min
60 min
C
+PLK-1KD
+PLK-1CA
SPD-5::RFP
10 μm
2 μm
0 s
15 s
75 s
255 s
540 s
condensate size (μm²)
time (min)
+PLK-1KD
+PLK-1CA
D
RFP mean intensity (normalized)
Time (s)
+PLK-1KD n=6
+PLK-1CA n=5
SPD-5::RFP
2 μm
High
Low
Pre-bleach
0 s
30 s
60 s
120 s
240 s
600 s
E
+PLK-1KD
+PLK-1CA
Pre Dilution
Post Dilution
SPD-5::RFP
5 μm
Normalized SPD-5::RFP PCM Mass
Pre
Post
Pre
Post
+PLK-1KD
+PLK-1CA

Figure 2

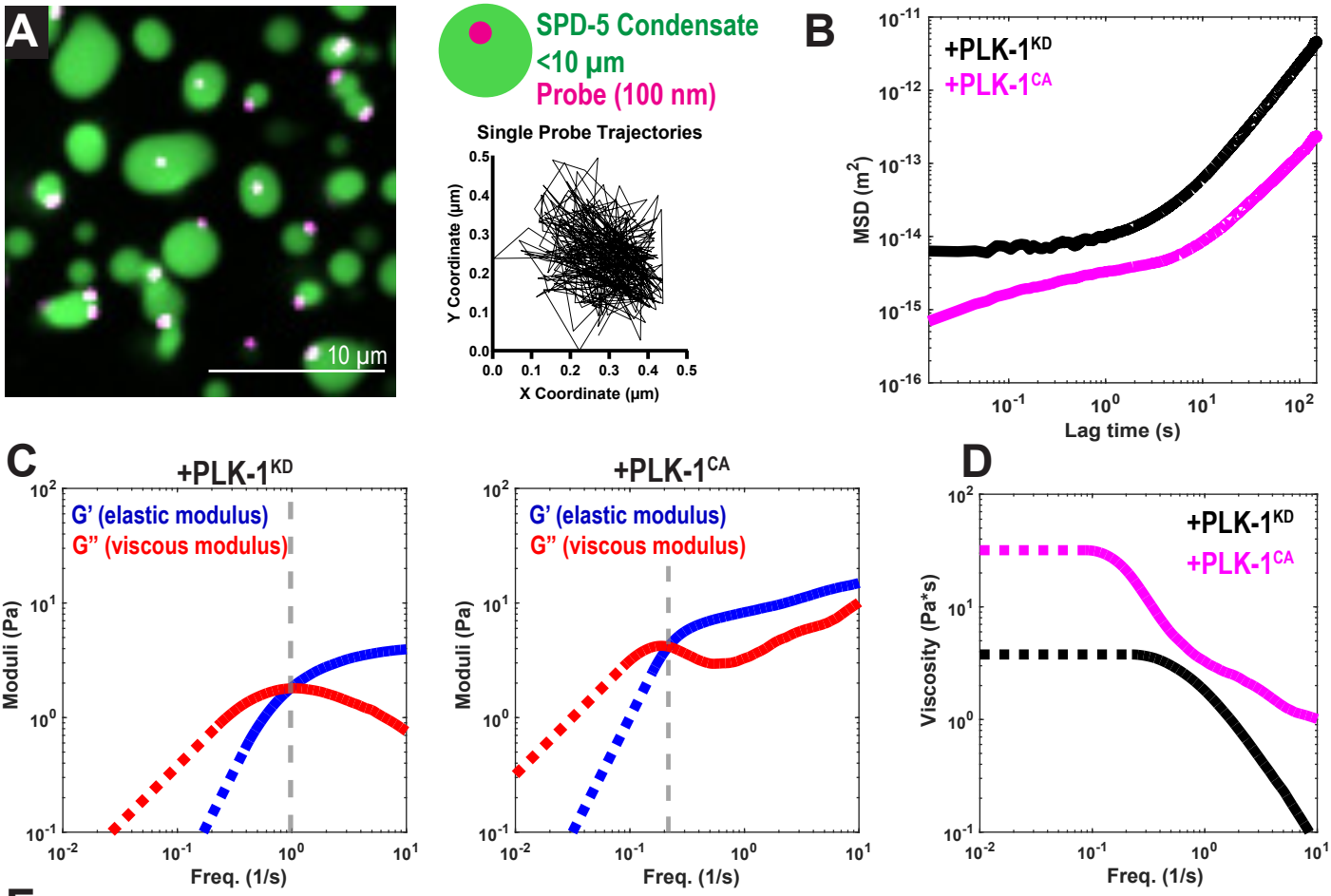

E

PLK-1 type	Crossover Point (1/s)	Zero Shear Viscosity (Pa•s)	Relaxation Time (s)	Condensate fusion	FRAP recovery	Resistance to dilution	Material State
KD	0.975	3.779	1.026	yes	low	low	more liquid-like
CA	0.217	31.84	4.616	no	none	high	more solid-like

Figure 3

A SPD-5 protein

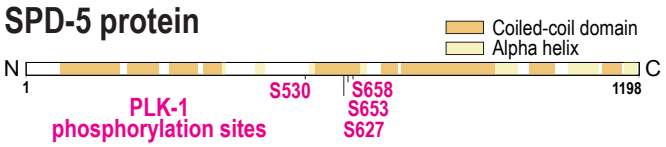

MosSCI strains

Chr I: endogenous *spd-5*

Chr II: GFP-labeled *spd-5* transgenes (RNAi resistant)

WT : S530, S627, S653, S658
4A : S530A, S627A, S653A, S658A phospho-null
4E : S530E, S627E, S653E, S658E phospho-mimic

B

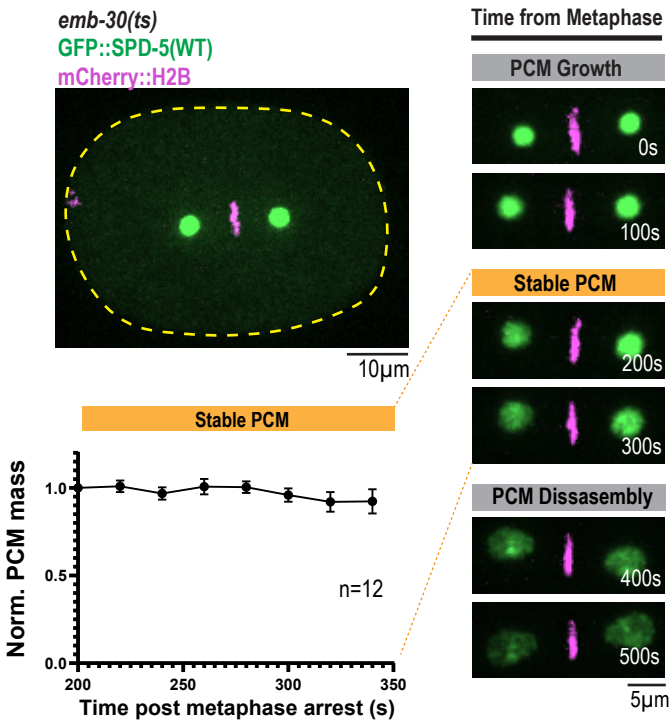

C

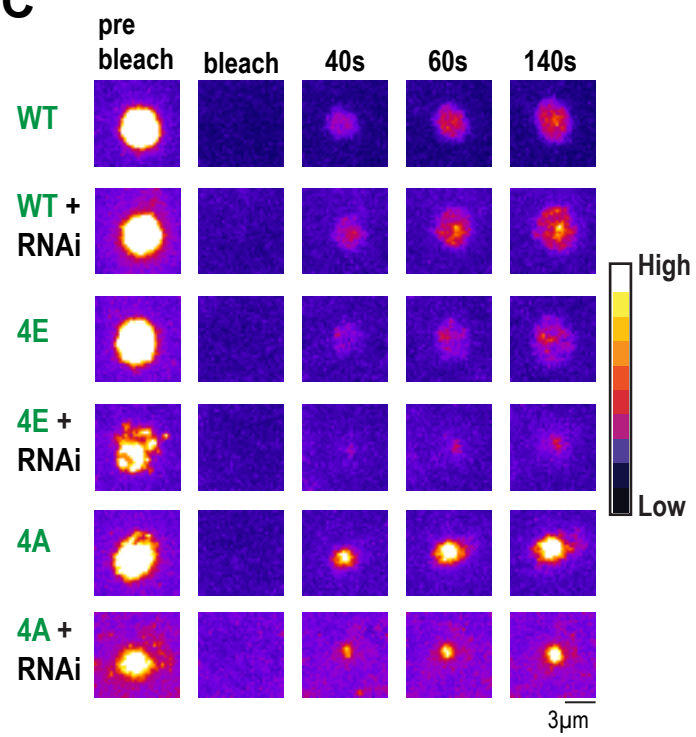

D

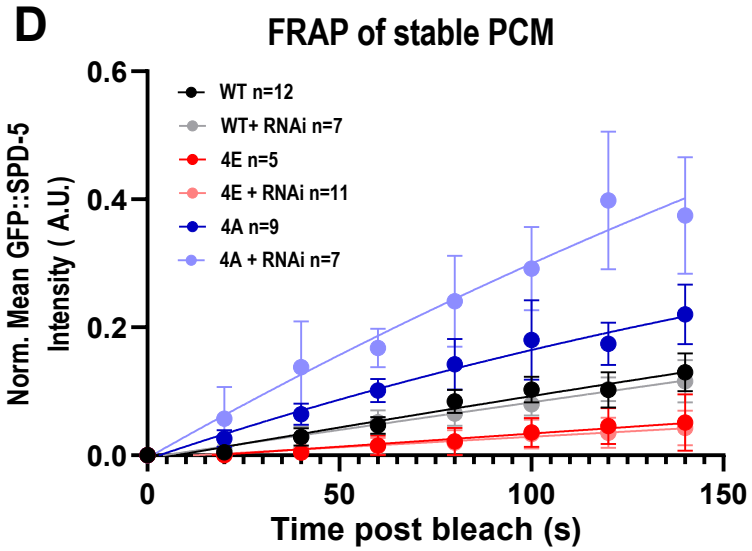

Figure 4

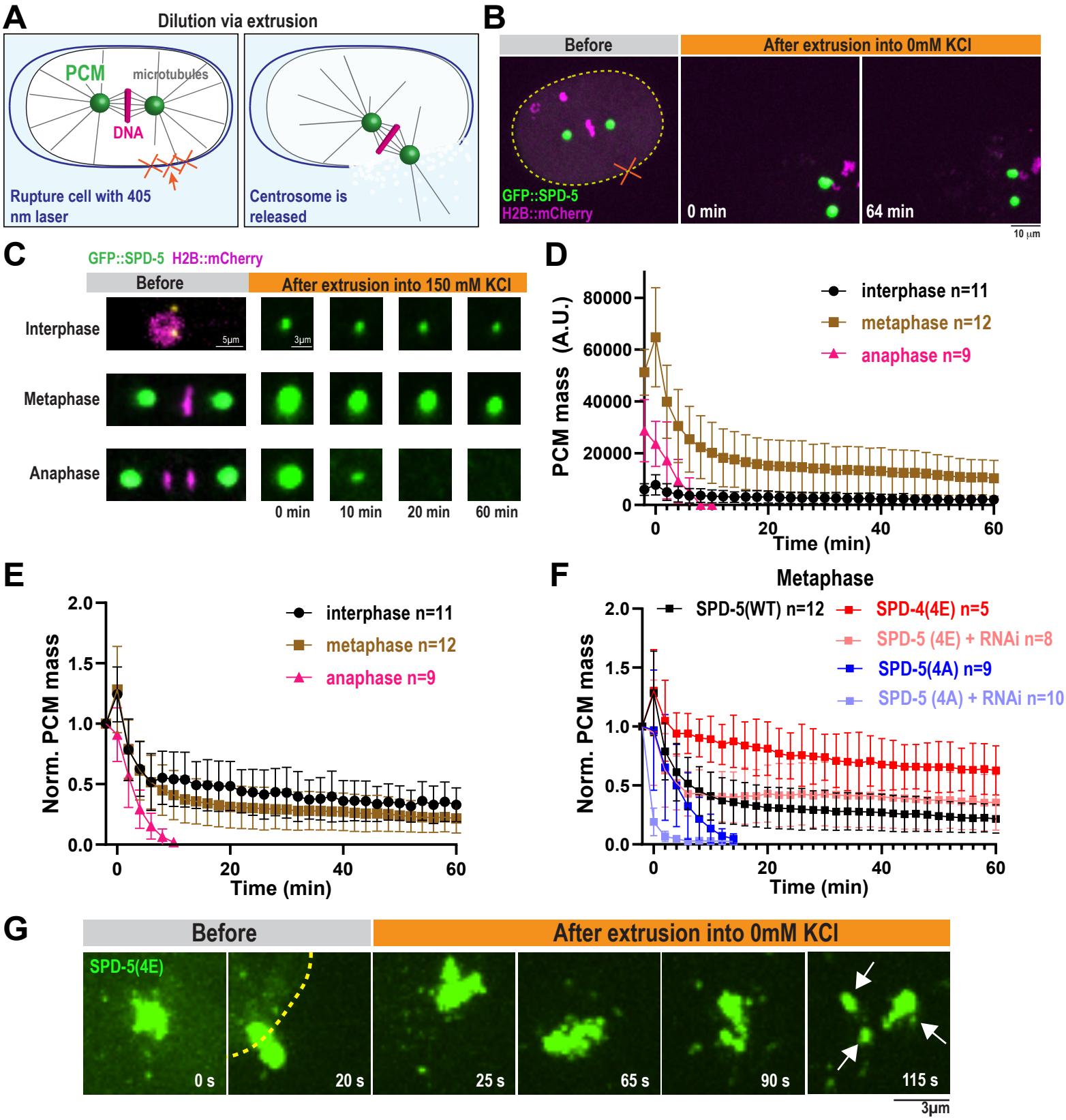
A
Dilution via extrusion
PCM
microtubules
DNA
Rupture cell with 405 nm laser
Centrosome is released
B
Before
After extrusion into 0mM KCl
GFP::SPD-5
H2B::mCherry
0 min
64 min
10 µm
C
GFP::SPD-5 H2B::mCherry
Before
After extrusion into 150 mM KCl
Interphase
Metaphase
Anaphase
5µm
3µm
0 min
10 min
20 min
60 min
D
PCM mass (A.U.)
Time (min)
interphase n=11
metaphase n=12
anaphase n=9
E
Norm. PCM mass
Time (min)
interphase n=11
metaphase n=12
anaphase n=9
F
Metaphase
Norm. PCM mass
Time (min)
SPD-5(WT) n=12
SPD-4(4E) n=5
SPD-5 (4E) + RNAi n=8
SPD-5(4A) n=9
SPD-5 (4A) + RNAi n=10
G
Before
After extrusion into 0mM KCl
SPD-5(4E)
0 s
20 s
25 s
65 s
90 s
115 s
3µm

Figure 5

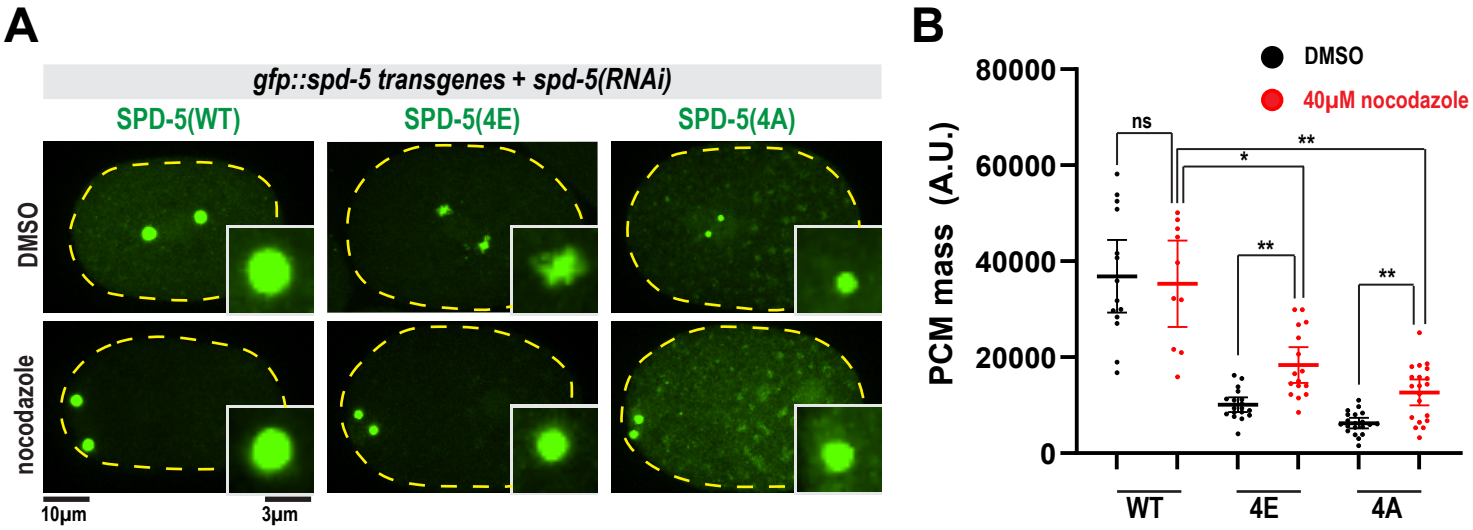
A
gfp::spd-5 transgenes + spd-5(RNAi)
SPD-5(WT)
SPD-5(4E)
SPD-5(4A)
DMSO
nocodazole
10µm
3µm
B
DMSO
40µM nocodazole
PCM mass (A.U.)
80000
60000
40000
20000
0
ns
*
**
**
**
WT
4E
4A

Figure 6

gfp::spd-5 transgenes + mCherry::H2B + spd-5(RNAi)

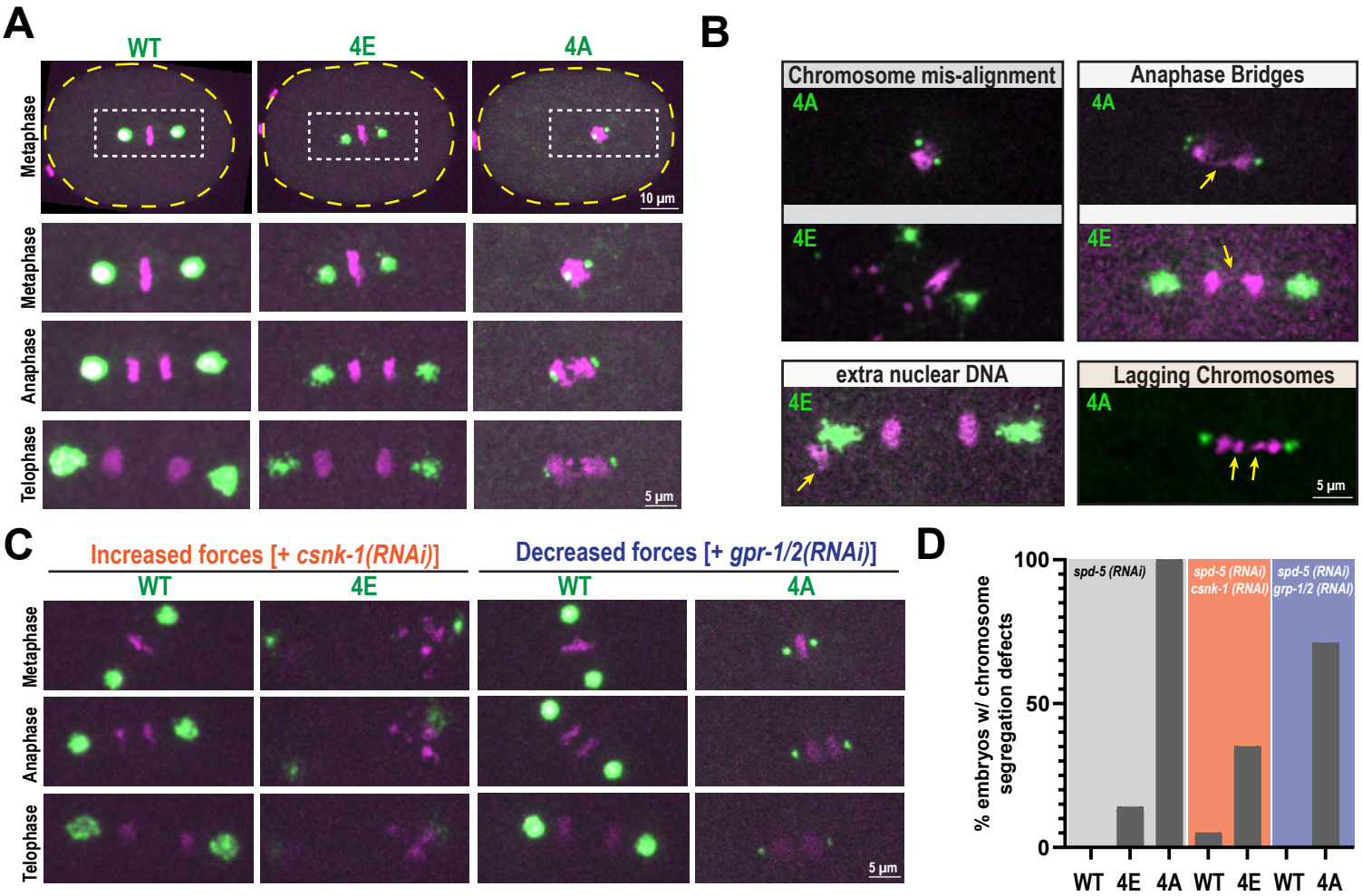

Figure 7

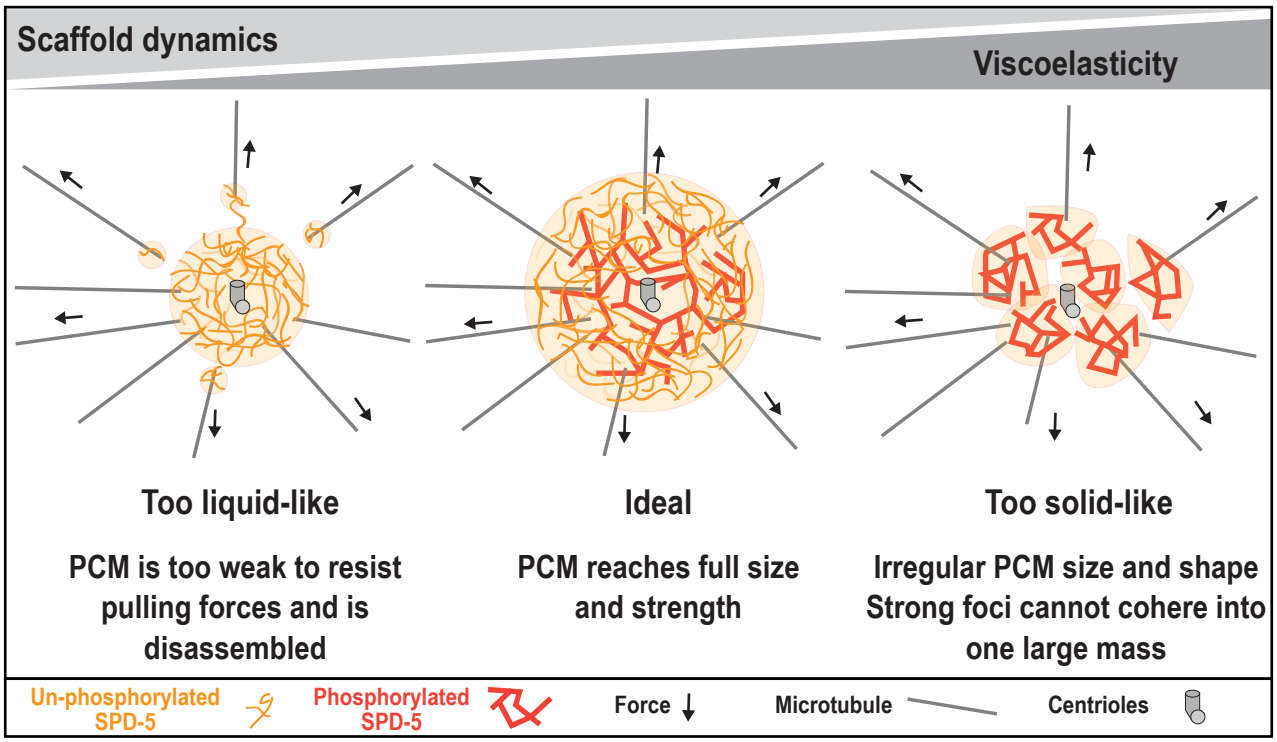
Scaffold dynamics
Viscoelasticity
Too liquid-like
PCM is too weak to resist pulling forces and is disassembled
Ideal
PCM reaches full size and strength
Too solid-like
Irregular PCM size and shape
Strong foci cannot cohere into one large mass
Un-phosphorylated SPD-5
Phosphorylated SPD-5
Force
Microtubule
Centrioles

Figure S1

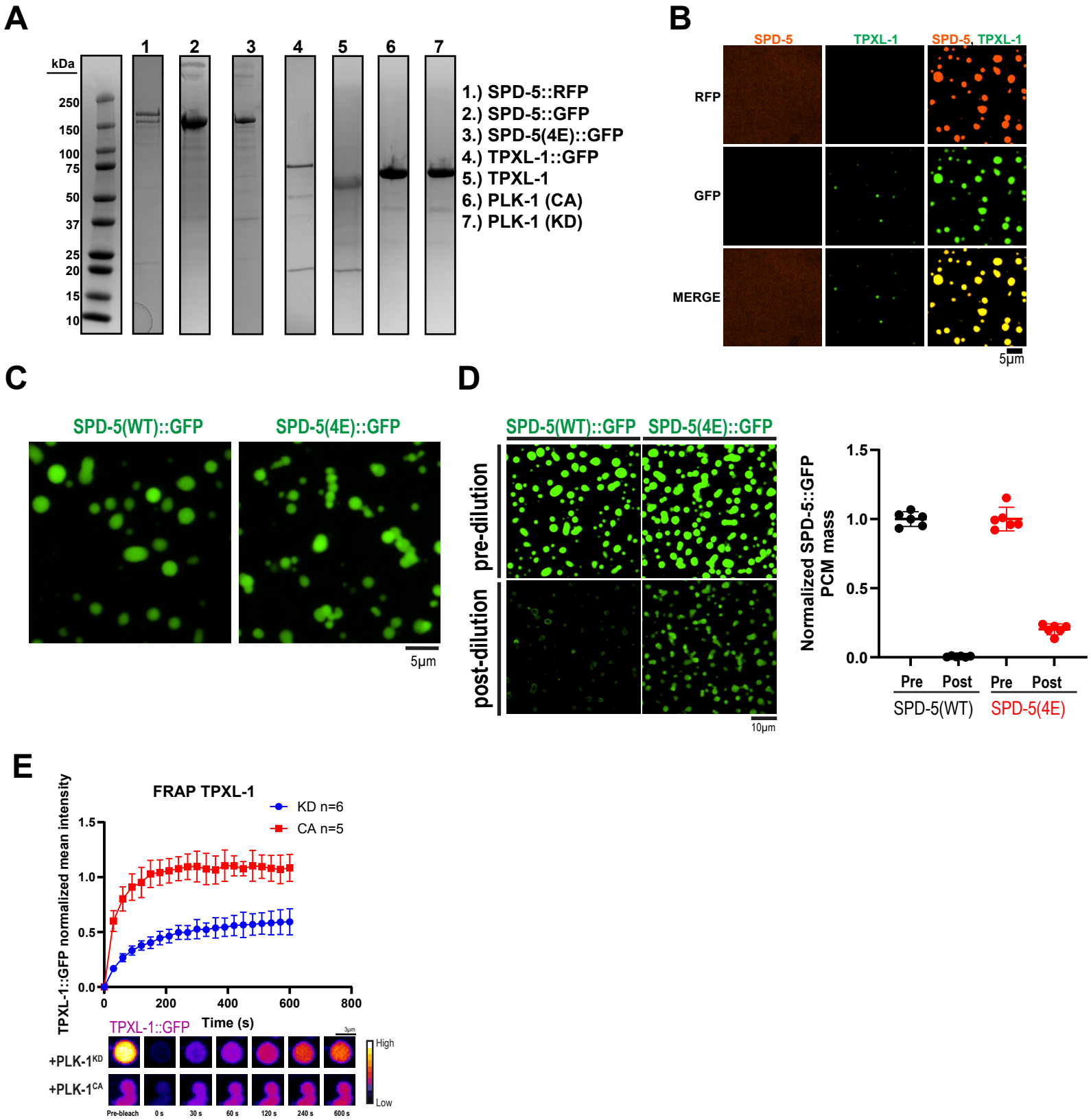
A
kDa
250
150
100
75
50
37
25
20
15
10
1 2 3 4 5 6 7
1.) SPD-5::RFP
2.) SPD-5::GFP
3.) SPD-5(4E)::GFP
4.) TPXL-1::GFP
5.) TPXL-1
6.) PLK-1 (CA)
7.) PLK-1 (KD)
B
SPD-5
TPXL-1
SPD-5, TPXL-1
RFP
GFP
MERGE
5µm
C
SPD-5(WT)::GFP
SPD-5(4E)::GFP
5µm
D
SPD-5(WT)::GFP
SPD-5(4E)::GFP
pre-dilution
post-dilution
10µm
Normalized SPD-5::GFP PCM mass
1.5
1.0
0.5
0.0
Pre
Post
Pre
Post
SPD-5(WT)
SPD-5(4E)
E
FRAP TPXL-1
KD n=6
CA n=5
TPXL-1::GFP normalized mean intensity
1.5
1.0
0.5
0.0
0
200
400
600
800
Time (s)
TPXL-1::GFP
3µm
+PLK-1KD
+PLK-1CA
High
Low
Pre-bleach
0 s
30 s
60 s
120 s
240 s
600 s

Figure S2

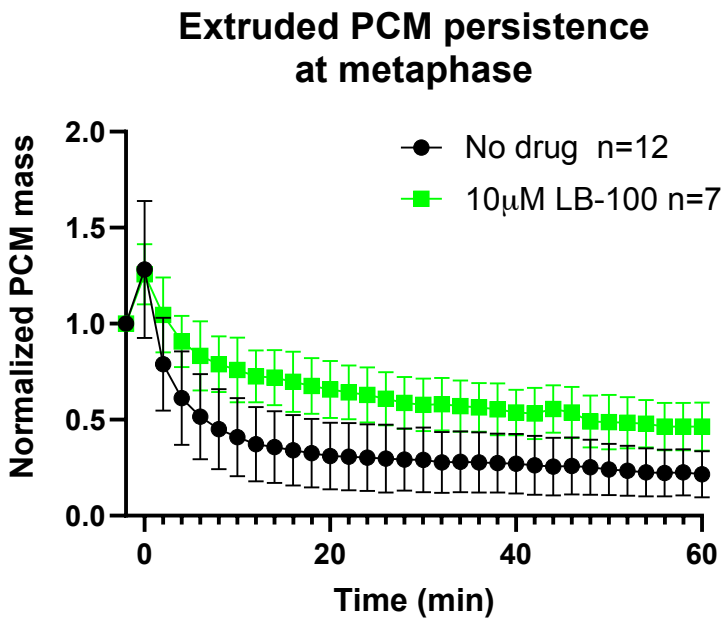
Extruded PCM persistence
at metaphase
No drug n=12
10μM LB-100 n=7
Normalized PCM mass
2.0
1.5
1.0
0.5
0.0
0
20
40
60
Time (min)

Figure S3

A

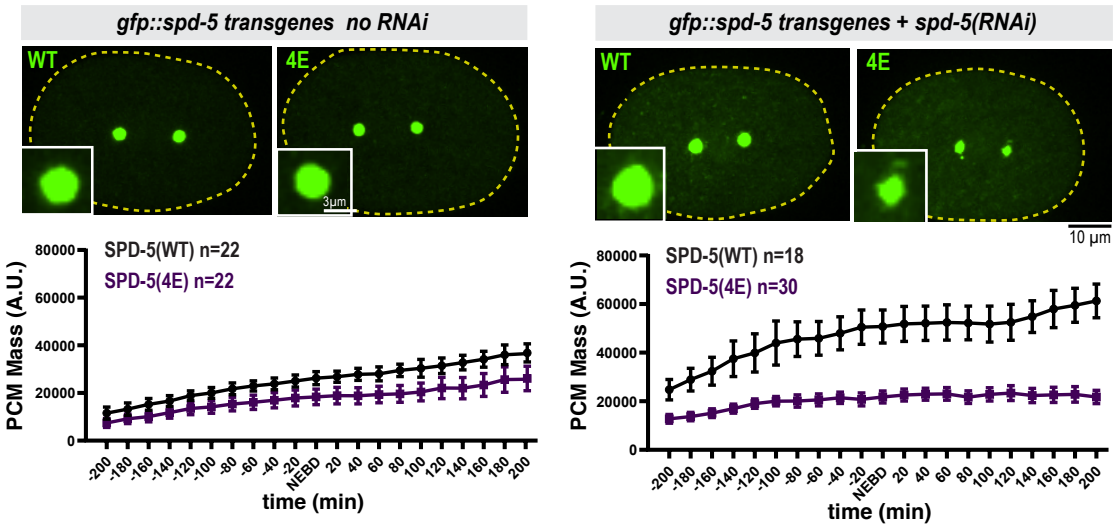

B

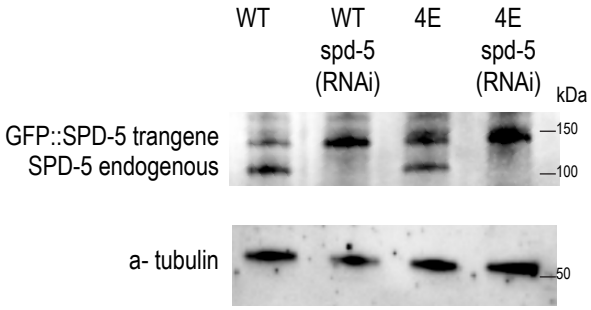

C

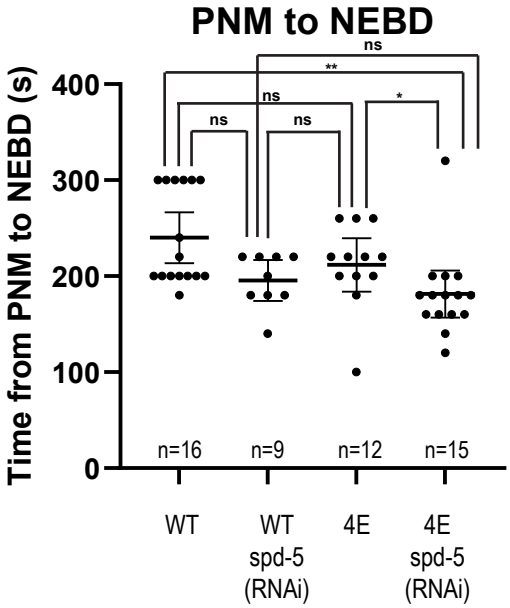

Figure S4

A

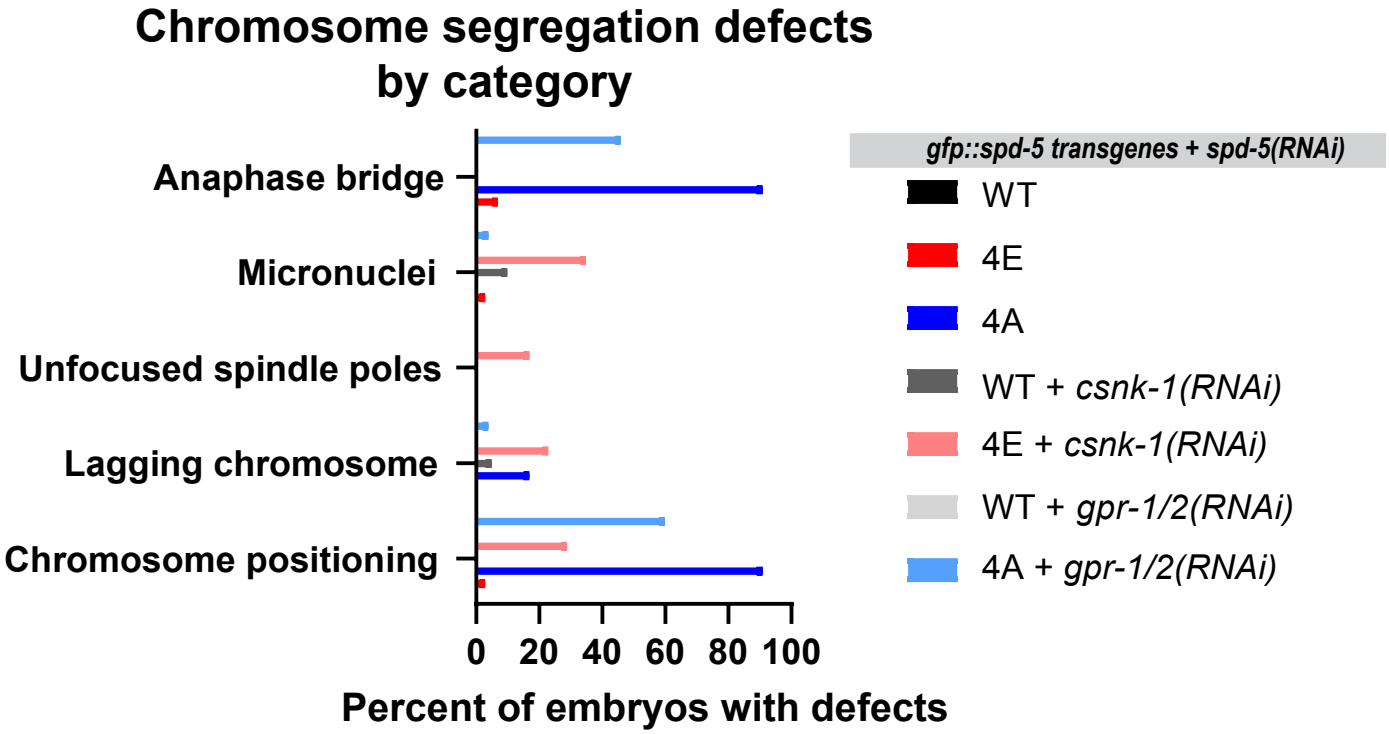

B

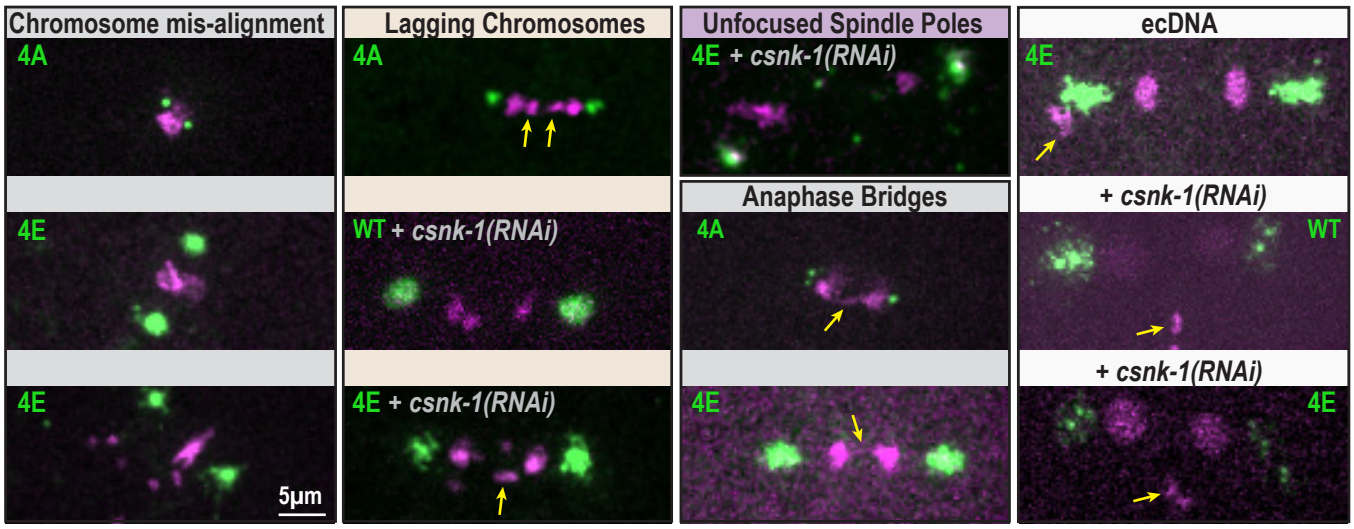

C

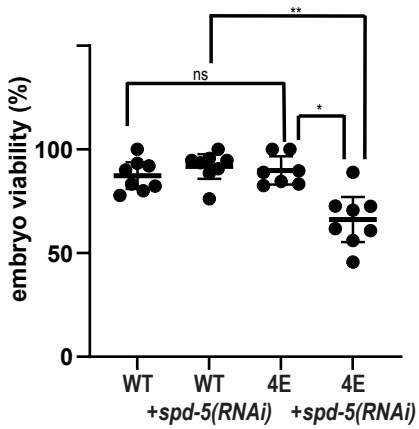

Figure S5

A

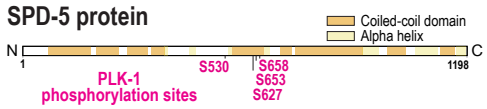

MosSCI strains

Chr I: endogenous *spd-5*

Chr II: GFP-labeled *spd-5* transgenes (RNAi resistant)

WT : S530, S627, S653, S658
4A : S530A, S627A, S653A, S658A — phospho-null
2A : S653A, S658A — expansion mutant
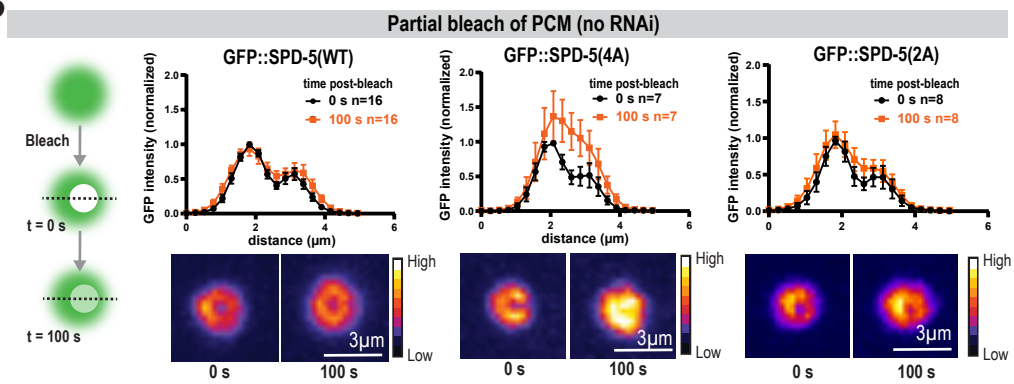
B